

(NASA-TM-81159) CONTROL SYSTEM DESIGNS FOR  
THE SHUTTLE INFRARED TELESCOPE FACILITY  
(NASA) 40 p HC A03/MF A01

N80-18869

CSCL 12B

Unclass

G3/66 47249

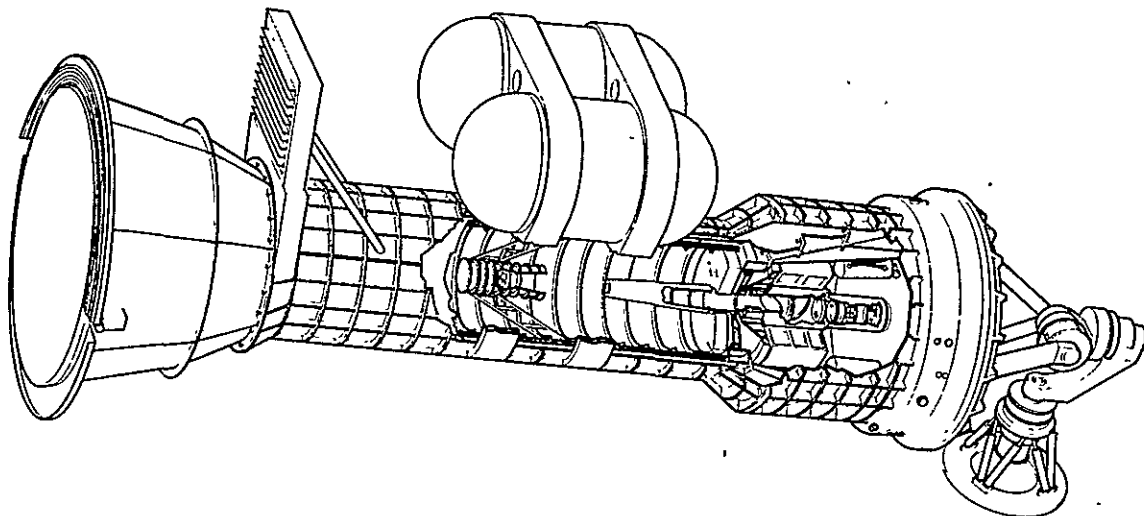
---

# Control System Designs for the Shuttle Infrared Telescope Facility

---

J. David Powell, Eric K. Parsons, and Kenneth R. Lorell

---



February 1980



---

# **Control System Designs for the Shuttle Infrared Telescope Facility**

---

J. David Powell

Eric K. Parsons, Stanford University, Stanford, California

Kenneth R. Lorell, Ames Research Center, Moffett Field, California



National Aeronautics and  
Space Administration

**Ames Research Center**  
Moffett Field, California 94035

## NOMENCLATURE

$a_0$	lateral acceleration of pivot, m/sec
$J_T$	telescope moment of inertia about pivot = 28,175 kg-m <sup>2</sup>
$K_B$	bending mode stiffness = 2.818×10 <sup>8</sup> Nm/rad
$K_D$	IPS rate feedback gain = 1.29×10 <sup>5</sup> Nm/(rad/sec)
$K_I$	IPS integral feedback = 3.42×10 <sup>5</sup> Nm/(rad-sec)
$K_p$	IPS proportional feedback = 5.7×10 <sup>5</sup> Nm/rad
$K_{\text{scale}}$	feed-forward scale factor = 1.0, nominally (0.95 for error analysis)
$M_T$	telescope mass = 2,140 kg
$r_T$	telescope center of mass offset = 2.5 m
$V_B$	bending mode damping = 2.818×10 <sup>4</sup> Nm/(rad/sec)
$\theta, \dot{\theta}$	IPS gimbal angle, rad, and angle rate, rad/sec
$\theta_B$	rotational bending error of secondary mirror, rad
$\theta_c, \dot{\theta}_c$	commanded pointing angle, rad, and rate, rad/sec
$\theta_g$	gyro output, rad
$\theta_I$	image angular position on focal plane, rad
$\theta_M$	commanded mirror angle, rad
$\omega_n$	gyro rate noise, rad/sec

# CONTROL SYSTEM DESIGNS FOR THE SHUTTLE INFRARED TELESCOPE FACILITY

J. David Powell and Eric K. Parsons

Guidance and Control Laboratory, Department of Aeronautics and Astronautics  
Stanford University, Stanford, Calif.

and

Kenneth R. Lorell  
Ames Research Center

## SUMMARY

The Shuttle Infrared Telescope Facility (SIRTF) is being designed as a 0.85-m, cryogenically cooled telescope capable of a thirtyfold improvement over currently available infrared instruments. The SIRTF, mounted in the Orbiter on the Instrument Pointing System (IPS), requires that the image at the focal plane be stabilized to better than 0.1 arcsec with an absolute accuracy of 1 arcsec in order to attain this goal. Current estimates of IPS performance for both stability and accuracy indicate that additional stabilization will be necessary to meet the SIRTF requirements. An Image Motion Compensation (IMC) system, utilizing a Charge Coupled Device (CCD) star tracker located at the focal plane and a steerable mirror in the SIRTF optical path, has been designed to work in conjunction with the IPS. The CCD tracks multiple stars simultaneously and through the use of a high-performance microcomputer generates three-axis attitude errors and gyro drift estimates to correct the IPS gyros. A high-bandwidth feed-forward loop, driven directly from the IPS gyro package, controls the steering mirror in order to correct disturbances not compensated for by the IPS control system. The SIRTF IMC system is described in detail and performance is analyzed with respect to system noise inputs, environmental disturbances, and error sources such as bending and feed-forward scale factor. It is concluded that the SIRTF accuracy and stability requirements can be met with this design.

## I. INTRODUCTION

The Shuttle Infrared Telescope Facility (SIRTF) is being designed as a 0.85-m, cryogenically cooled, infrared telescope to be flown as a Shuttle-attached payload in the mid-1980's (ref. 1). The SIRTF, mounted in the Orbiter bay on the European Instrument Pointing System (IPS), will make possible previously unobtainable photometric and spectrographic observations over a wide range of IR wavelengths (ref. 2).

In order to maximize the effectiveness of SIRTF as a scientific instrument, the optical axis must be pointed with an absolute accuracy of 1 arcsec and the image at the focal plane must remain stable to 0.1 arcsec (ref. 3). The signal-to-noise ratio during the observation of faint sources is further enhanced by chopping the incoming beam with an oscillating mirror located in the optical train. The modulated image has the same accuracy and stability requirements as the unchopped

one. These stringent pointing and stability requirements are further complicated by the demands that infrared astronomy, and the SIRTF in particular, places on the design of the pointing system.

Primary among the factors that add complexity to the analysis and design of the SIRTF controller are the telescope's cryogenically cooled optics, which are required to avoid thermal interference with the extremely sensitive IR detectors at the focal plane. The entire internal structure of the telescope operates at a temperature of 8 K and below. This low temperature is made possible by a concentric shell design in which the inner optical portion of the telescope is connected to the outer structural cylinder by thin, thermally resistive members, thus minimizing heat-transfer losses (ref. 4). Unfortunately, the mechanical coupling between the SIRTF mounting fixture and the optical system is relatively light and flexible, making precise knowledge of the optical axis uncertain.

A second difficulty peculiar to infrared astronomy, and the source of a major shortcoming of previous IR telescope pointing systems, is the lack of a visible component associated with many infrared objects. These objects are therefore not visible to the astronomer, nor can the pointing system use them for augmentation of the basic gyrostabilization loops as is often done in optical astronomy. Tracking a nearby visible object is of course possible, but multiple star trackers are then required to provide three-axis error information. Even when multiple star trackers are used to provide the off-axis tracking function, the problems of target identification and limited interaction with the control system still remain.

The SIRTF will be mounted on the IPS in the Orbiter bay. The most recent simulations of IPS operation have indicated that although quiescent performance is in the 1- to 2-arcsec range, disturbance errors may be as large as 3 arcsec (ref. 5). Thus, although the IPS can provide positioning for target acquisition and a stable base to isolate the SIRTF from large-amplitude Shuttle disturbances, it does not provide the necessary pointing precision and image stability for the SIRTF. Additionally, the image-dissector-tube star trackers used by the IPS have no star-field display capability.

It is apparent, therefore, that a number of challenging design problems pertain to the operation of an infrared telescope mounted on the IPS. They are:

1. The thermal distortion due to temperature differentials between the inner and outer telescope sections
2. The light and flexible mechanical coupling between the inner and outer telescope shells
3. The difficulty of providing off-axis pointing using current star tracker systems
4. The lack of a star-field display for the operator
5. The inability of the IPS to meet the SIRTF fundamental pointing and stability requirements

The present work deals with the development of an image motion compensation (IMC) system, internal to the SIRTF, that provides the stability and control to meet the SIRTF's pointing requirements. The IMC system uses a charge coupled device (CCD) array, located at the SIRTF focal plane, and outputs from the IPS gyros to drive a mirror in the telescope optical train. The operation of the

CCD and the IMC system is controlled by a high-performance microcomputer whose extremely fast cycle time permits multiple stars to be tracked and error commands to be calculated for all three axes.

The SIRTF IMC is based in part on the Video Inertial Pointing (VIP) system developed between 1974 and 1977 at Ames Research Center (refs. 6 and 7). The VIP system also used a CCD to track multiple stars and combined the star-tracker information with gyro outputs. However, the concept of steering a mirror inside the telescope is a major difference between VIP and the SIRTF/IMC. In part, the steering mirror concept evolved due to the stringent SIRTF pointing requirements and because a movable mirror was already part of the SIRTF optical design.

## II. SYSTEM DESCRIPTION

The SIRTF/IMC system operates by combining the outputs of the IPS gyros with measurements from a CCD array at the telescope focal plane. The gyros provide a high bandwidth, low-noise signal yielding good short-term stability; the much noisier CCD array provides the long-term stability. The result is a system that possesses the desirable characteristics of both devices. The combined signal is used to compensate the focal plane image by moving a two-axis steerable mirror in the SIRTF optical system.

The readout and control of the 500×500-element CCD is performed by a high-performance microcomputer built into the SIRTF on-board electronics. The computer accepts raw video data from the CCD, performs an interpolation algorithm in order to effectively enhance the CCD resolution (ref. 8), and generates a pointing-error signal for each of the three axes based on the relationship between the desired and the current positions of the tracked stars in the CCD field of view (ref. 9).

Thus, a precise measure is available from the CCD of the current orientation of the telescope optical axis, irrespective of thermal mechanical distortion, or external star-tracker alignment. The error signal derived from this measurement is processed by a Kalman filter in the SIRTF microcomputer to correct the gyro outputs, both in pointing offset and drift. The time constant for these error corrections is naturally quite long, of the order of tens of seconds (or hundreds of seconds when tracking  $M_v + 14$  stars).

The problem of short-term, high-bandwidth stability is solved by controlling the image with a gimballed mirror which functions as the secondary mirror in the Cassegrain optical system of the SIRTF. Using this mirror as an image-steering device is a natural application since it already must have a high-performance servo system in order to spatially chop the image.

Any motion of the IPS-SIRTF sensed by the gyros but not corrected for by the IPS controller will be compensated by moving the steering mirror. The IMC system acts to increase the system bandwidth by acting on disturbances to which the IPS cannot respond. The steering mirror is driven directly in a feed-forward mode by the IPS gyro outputs. This feed-forward loop provides two important advantages: (1) the bandwidth is limited only by the bandwidth of the gyro and of the mirror servo, not the closed-loop system bandwidth of the IPS-SIRTF; and (2) the possibility of a SIRTF structural resonance exciting a control system instability is eliminated because there is no

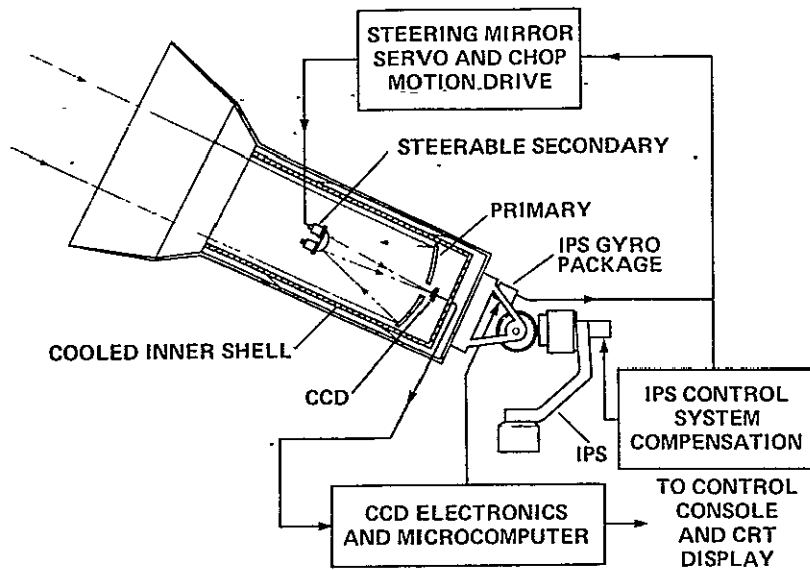


Figure 1.— Schematic of the SIRTF IMC system.

direct closed loop between the sensor and actuator. Feed-forward loops are, of course, sensitive to errors in scale factor. An analysis of the effects of scale-factor error has been performed for this system and is discussed in a later section.

Figures 1 and 2 are schematic and block diagrams, respectively, of the IMC system. Note the direct interfaces between the SIRTF microcomputer, the IPS three-axis gyro package, and the steering mirror. The entire system is coupled to the SIRTF control console in order to provide the operator with a video star-field display, control of the telescope optical axis, and CCD operational parameters (e.g., threshold, integration time, and number of tracked stars) (see ref. 10).

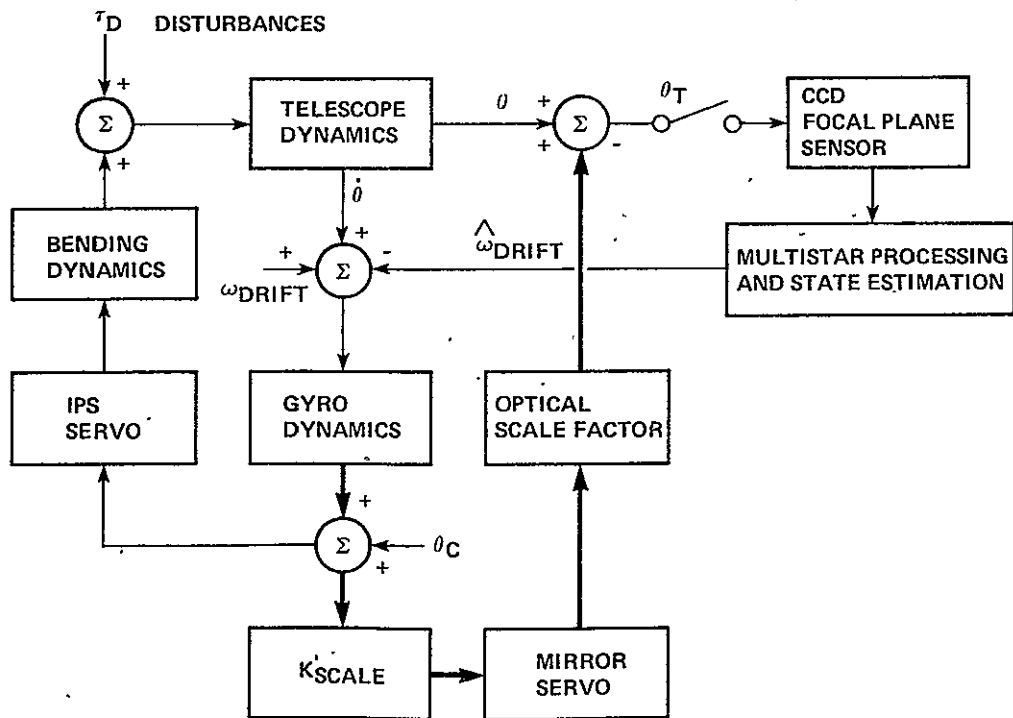


Figure 2.— Block diagram of the SIRTF/IMC system.

### III. ANALYSIS OF THE IMAGE-MOTION COMPENSATION SYSTEM

A number of system- and environment-related factors were involved in the design and performance analysis of the IMC system. The fundamental problem was one of synthesizing a system that would be insensitive to a variety of noise and disturbance inputs, yet one that could operate with the limitations imposed by tracking  $M_V + 14$  stars. For the purposes of analysis, the telescope and IPS system were considered to be continuous. Actually, the IPS feedback control law is to be digital with a sample rate of 50 Hz; however, this is considerably faster than the digital state estimation loop, which is performed at sample rates as low as 0.1 Hz; therefore, it is reasonable to assume the IPS dynamics to be continuous for analysis of behavior substantially slower than 50 Hz.

Once a design concept utilizing a combination of digital and continuous loops had been established, the analysis proceeded along two distinct paths: (1) the inspection of the response of the continuous portion of the system to Shuttle disturbance torques, feed-forward scale-factor error, and gyro-rate noise; and (2) optimization of the discrete portion of the system in order to minimize errors from CCD noise, long-term gyro drift, and thermal distortion. Modeling of the system was done only for the single-axis case; however, accurate numerical data to the greatest extent possible were obtained for all relevant CCD, IPS, and Shuttle parameters to make the results realistic and useful.

#### 3.1 Continuous-Loop Equations of Motion

The governing equations of motion for the continuous portion of the system are:

$$-J_T \ddot{\theta} = J_T \ddot{\theta}_B + V_B \dot{\theta}_B + K_B \theta_B + M_T r T a_o \quad (1)$$

$$V_B \ddot{\theta}_B = -K_B \dot{\theta}_B + K_I (\theta_g - \theta_c) + K_p \left[ \omega_n + \ddot{\theta} - \dot{\theta}_c - \frac{d}{dt} (\theta_c) \right] + K_D \left[ \dot{\omega}_n - \frac{d}{dt} (\dot{\theta}_c) + \ddot{\theta} \right] \quad (2)$$

$$\dot{\theta}_g = \omega_n + \dot{\theta} - \dot{\theta}_c \quad (3)$$

$$\theta_I = \theta + 2\theta_B - 2\theta_M \quad (4)$$

$$\theta_M = \frac{K_{\text{scale}}}{2} (\theta_g - \theta_c) \quad (5)$$

As can be seen from the schematic diagram in figure 3, equation (1) represents the telescope dynamics. Figure 3 also shows the geometric aspects of the bending model. Specifically, the gyro mounting orientation and the CCD focal plane are assumed fixed to each other. Furthermore, since the gimbal is assumed to be massless, the torquer acts instantaneously so that it balances the torque from the spring deflection and damping. This last relation is expressed in equation (2) with the IPS control torque expanded in terms of its components. Equation (4) relates to focal plane image with telescope attitude and mirror attitude changes. It reflects the fact that with the geometry

IMAGE POSITION IN FOCAL PLANE:  $\theta_T = \theta + 2\theta_B - K_{SCALE}(\theta_g - \theta_c)$

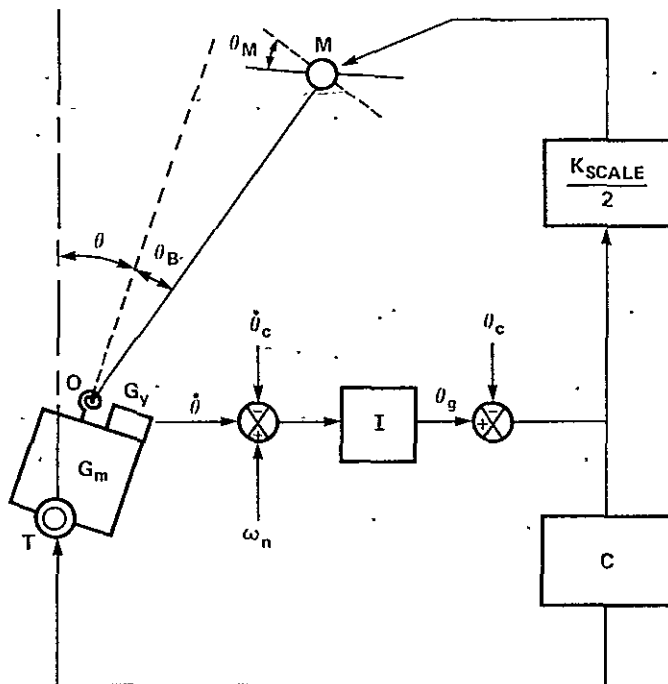


Figure 3.— Telescope/IPS bending model schematic diagram.

shown in figure 3, the optical scale factor of the system is 2. It is possible that in the final configuration the optics may not be structured so that the relation between mirror angle and image motion has this value. Equation (5) reflects this same value (2) of the optical scale factor.

All the equations are contained in the system block diagram shown in figure 4.

In the following section, these system dynamics will be used to determine frequency responses to Shuttle accelerations and gyro noise. The transfer functions to be used in the frequency response analysis follow directly from equations (1) through (5); they are:

$$\begin{bmatrix}
 \frac{\theta(s)}{a_O(s)} & \frac{\theta(s)}{\omega_n(s)} \\
 \frac{\theta_B(s)}{a_O(s)} & \frac{\theta_B(s)}{\omega_n(s)} \\
 \frac{\theta_g(s)}{a_O(s)} & \frac{\theta_g(s)}{\omega_n(s)} \\
 \frac{\theta_I(s)}{a_O(s)} & \frac{\theta_I(s)}{\omega_n(s)}
 \end{bmatrix} = \frac{
 \begin{bmatrix}
 -\frac{M_T t T}{J_T} s(V_B s + K_B) & -\frac{1}{s} (K_D s^2 + K_p s + K_I) s^2 + \frac{V_B}{J_T} s + \frac{K_B}{J_T} \\
 -\frac{M_T r T}{J_T} (K_D s^2 + K_p s + K_I) & s(K_D s^2 + K_p s + K_I) \\
 -\frac{M_T r T}{J_T} s(V_B s + K_B) & s^2 (V_B s + K_B) \\
 -\frac{M_T r T}{J_T} [(1 - K_{\text{scale}})s(V_B s + K_B) & \frac{1}{s} (K_D s^2 + K_p s + K_I) \\
 + 2(K_D s^2 + K_p s + K_I)] & \cdot s^2 - \frac{V_B}{J_T} s - \frac{K_B}{J_T} - K_{\text{scale}} \\
 & \cdot s^2 (V_B s + K_B)
 \end{bmatrix}}{(V_B s + K_B) \left( s^3 + \frac{K_D}{J_T} s^2 + \frac{K_p}{J_T} s + \frac{K_I}{J_T} \right) + s^2 (K_D s^2 + K_p s + K_I)}$$

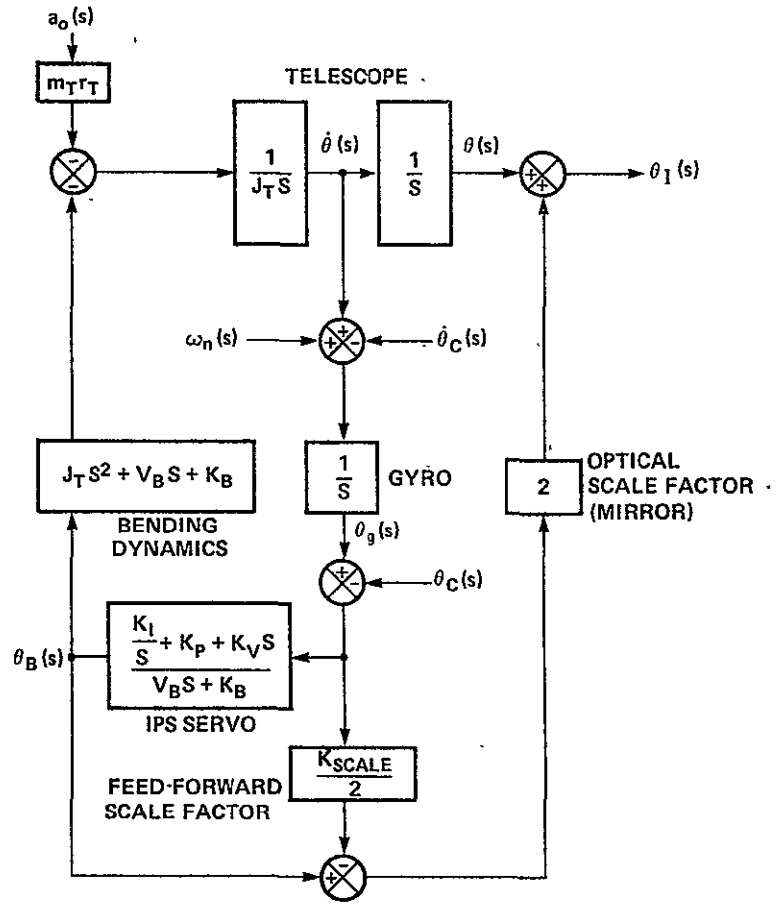


Figure 4.— Block diagram of the continuous portion of the IMC system.

### 3.2 Discrete-Loop Difference Equations

Figure 4 shows the focal plane image as  $\theta_I(s)$ . The CCD measurement is an average of the image motion over the CCD integration interval; hence, if the rate of image motion is assumed constant over one integration interval,

$$\theta_{CCD}(i+1) = \frac{\theta_I(i+1) + \theta_I(i)}{2} \quad (7)$$

where  $\theta_{CCD}$  is the measured value of  $\theta_I$  from the CCD. Using z-transforms, equation (7) can be written

$$\frac{\theta_{CCD}(z)}{\theta_I(z)} = \frac{z+1}{2z} \quad (8a)$$

An approximate transfer function

$$\frac{\theta_{CCD}(s)}{\theta_I(s)} = \frac{1/T}{s + 1/T} \quad (8b)$$

models CCD attenuation of high-frequency image motion.

The image-motion compensation system consists of feed-forward of gyro-measured attitude to the steerable mirror. If there is no scale-factor error between gyro-measured attitude and the image motion caused by the mirror angle commands, the image-motion errors will be solely due to gyro noise and drift and to the structural bending that occurs at a higher frequency than the CCD bandwidth. The goal of the discrete compensation system is to estimate gyro error from the CCD measurements. The estimates are used to correct the telescope attitude, image position, and gyro attitude measurement. The controller uses the outputs of a state estimator for the angle error  $\theta_D$  and the drift  $D$ , to form the gyro rate command:

$$\dot{\theta}_c = \frac{1}{T} \theta_D + D \quad (9)$$

Within the limitations of scale error and bending, the image-motion follows the gyro output. Thus, after one integration interval the controlled image position is

$$\theta_{I_{i+1}} = \theta_{D_{i+1}} + \hat{\theta}_{D_i} + \hat{D}_i T \quad (10)$$

The image response to gyro drift is negative because the IPS integral control causes the telescope to drift so as to null the rate input of the gyro.

Ignoring for now the gyro noise characteristics, the dynamic equations for drift, including the control, are

$$\begin{bmatrix} \theta_D \\ D \\ \theta_{CCD} \end{bmatrix}_{i+1} = \begin{bmatrix} 1 & T & 0 \\ 0 & 1 & 0 \\ -1 & -T/2 & 0 \end{bmatrix} \begin{bmatrix} \theta_D \\ D \\ \theta_{CCD} \end{bmatrix}_i + \begin{bmatrix} -K_g T & -T \\ 0 & 0 \\ K_g T/2 & T/2 \end{bmatrix} \begin{bmatrix} \hat{\theta}_D \\ \hat{D} \end{bmatrix}_i + \text{gyro noise terms} \quad (11)$$

where  $K_g = 1/T$ .

The estimate equations reduce to

$$\begin{bmatrix} \hat{\theta}_D \\ \hat{D} \\ \hat{\theta}_{CCD} \end{bmatrix}_{i+1} = \begin{bmatrix} 0 & 0 & 0 \\ 0 & 1 & 0 \\ -1/2 & 0 & 0 \end{bmatrix} \begin{bmatrix} \hat{\theta}_D \\ \hat{D} \\ \hat{\theta}_{CCD} \end{bmatrix}_i + \begin{bmatrix} K_1 \\ K_2 \\ K_3 \end{bmatrix} \left\{ \theta_{CCD_{i+1}} - \bar{\theta}_{CCD_{i+1}} \right\} \quad (12)$$

where

$$\bar{\theta}_{CCD_{i+1}} = -(1/2)\hat{\theta}_{D_i}$$

The following transfer functions are derived from the drift and estimate equations given above:

$$\left. \begin{aligned} \frac{\theta_D(z)}{D(z)} &= \frac{T}{z-1} \\ \frac{\hat{\theta}_D(z)}{\hat{D}(z)} &= \frac{-1}{z-1} \\ \frac{\theta_D(z)}{\hat{D}(z)} &= \frac{-T}{z-1} \\ \frac{\theta_{CCD}(z)}{\theta_D(z)} &= \frac{-(z+1)}{2z} \\ \frac{\hat{\theta}_D(z)}{\theta_{CCD}(z)} &= \frac{K_1}{z-K_1/2} \\ \frac{\hat{D}(z)}{\theta_{CCD}(z)} &= \frac{K_2 z}{(z-1)(z-K_1/2)} \\ \frac{\hat{\theta}_{CCD}(z)}{\theta_{CCD}(z)} &= \frac{K_3 z - K_1/2}{(z-K_1/2)z} \end{aligned} \right\} \quad (13)$$

The discrete compensation consists of processing the  $\theta_{CCD}$  measurements in the estimator (eq. (12)) and then combining the state estimates to torque the gyro by equation (9). Combining these equations in transfer function form results in:

$$\frac{\dot{\theta}_c(z)}{y(z)} = \frac{(K_1 + TK_2)z - K_1}{(z-1)(z-K_1/2)} \quad (14)$$

where  $y = \theta_{CCD} + \text{noise}$ .

The discrete compensation is contained within the dashed lines of figure 5. The discrete model of the gyro, mirror command to image motion, and CCD response are also shown to complete the block diagram for the discrete feedback loop. The noise input  $\omega_i$  provides the discrete equivalent of the long-term drift rate; it is described in the following section. An optimal filter, discussed subsequently, also has the form of equation (14). The interpretation of the Kalman gains for the optimal filter must be modified because the term  $-(T^2/6)\omega_i$  causes the noise in the measurement  $y$  to be

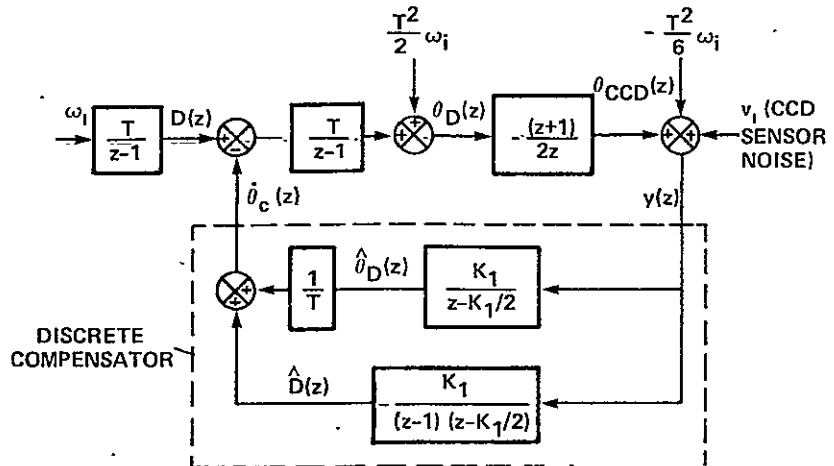


Figure 5.— Discrete-loop block diagram.

correlated with the random-walk driving random sequence. The goal of optimum estimation is minimum variance estimates of drift and drift rate in the presence of sensor noise. Some of the sensor noise characteristics described in reference 10 are summarized below.

### 3.3 Sensor Noise Model

Gyro noise is modeled as a combination of high-frequency rate noise and long-term random-walk drift. Characteristics of three candidate Instrument Pointing System gyros, documented in appendix A of reference 10, are summarized in table 1.

TABLE 1.- GYRO CHARACTERISTICS

Gyro model	Integrated rate noise, arcsec rms	Random-walk drift rate after 1 hr, arcsec/sec rms
Hamilton Standard RI-1139	0.11	0.01
Bendix 64 PM	.11	.0005
Ferranti 125	.017	.0005

The integrated rate noise is the noise in the image position on the focal plane. This noise is completely transmitted into the angular position of the line of sight by the high-bandwidth mirror control and therefore fundamentally limits the pointing accuracy. High-frequency gyro noise is attenuated by the effective CCD transfer function (eq. (8b)) whose break frequency varies inversely with CCD integration time. The resulting rms noise in the CCD measurement is shown in figure 6. These values are generally lower than the intrinsic CCD sensor noise shown in figure 7, which is taken from reference 10 and repeated here for completeness. The error covariance of gyro-related noise can be obtained from figure 6 and added to the CCD sensor noise covariance from figure 7.

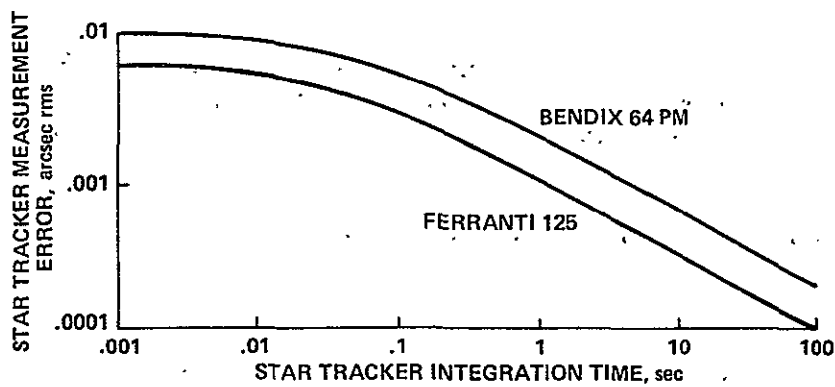


Figure 6.— Star-tracker measurement error resulting from gyro rate noise.

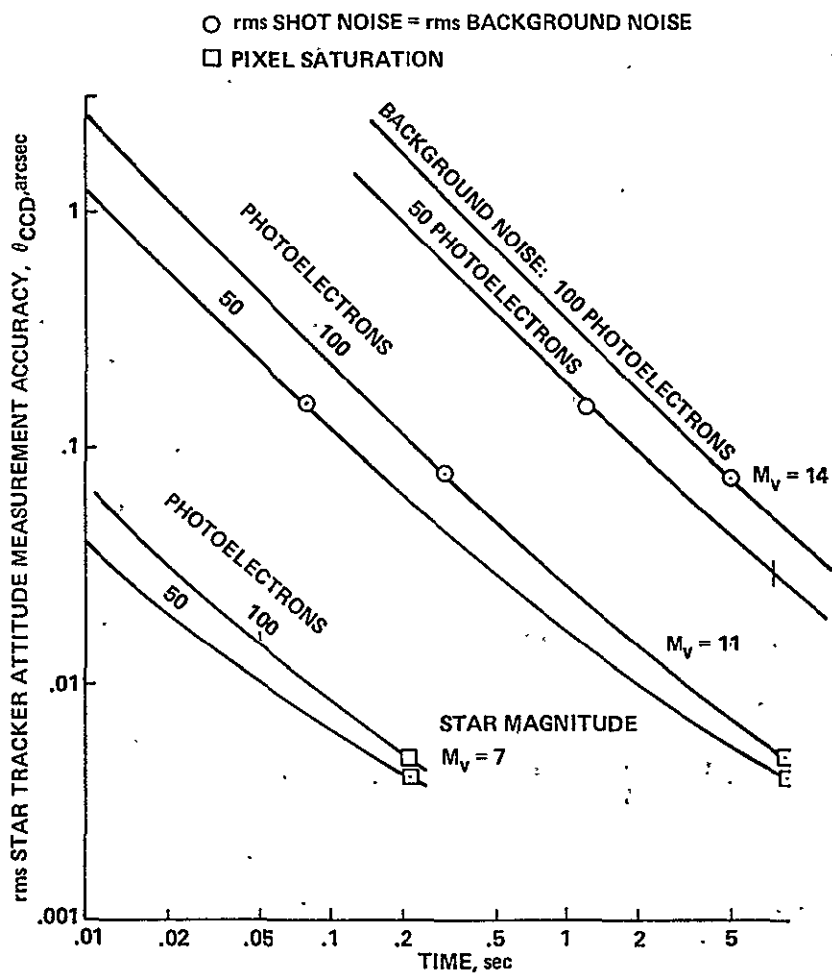


Figure 7.— Sample-to-sample error of star-tracker measurement of image centroid for a 15-arcmin field of view (ref. 10).

It remains to evaluate the gyro noise terms appearing in equation (11). These are the contribution of long-term random-walk drift that is modeled by integrated white noise. The error covariance of the driving white noise is determined so that the rms random-walk drift is equal to the quoted long-term drift after an elapsed time of 1 hr.

The continuous random-walk process is modeled by:

$$\dot{D} = \omega \quad (15)$$

where  $D$  is the random-walk drift and  $\omega$  is the purely random driving noise. The discrete equivalent of equation (15) is

$$D_i = D_{i-1} + T\omega_i \quad (16)$$

The error covariance equation corresponding to equation (16) is:

$$\langle D_i^2 \rangle = \langle D_{i-1}^2 \rangle + T^2 Q \quad (17)$$

or

$$\langle D_i^2 \rangle = \langle D_0^2 \rangle + iT^2 Q \quad (17)$$

where  $i$  = the  $i$ th time interval;  $T$  = the length of the time interval;  $Q = \langle \omega_i^2 \rangle$ ; and  $\langle \rangle$  = an ensemble average of the random variable. If  $D_0$  is the nominal gyro drift, then using equation (17) over the desired time span of 1 hr, or 3,600 sec:

$$\left. \begin{aligned} \langle D_{3600/T}^2 \rangle - \langle D_0 \rangle^2 &= D_0^2 = \frac{3600}{T} T^2 Q \\ \Rightarrow Q &= D_0^2 / 3600T \end{aligned} \right\} \quad (18)$$

The contribution of random-walk drift to pointing error is then modeled by

$$\begin{Bmatrix} \theta_D \\ D \end{Bmatrix}_{i+1} = \begin{bmatrix} 1 & T \\ 0 & 1 \end{bmatrix} \begin{Bmatrix} \theta_D \\ D \end{Bmatrix}_i + \underbrace{\begin{bmatrix} K_g T & -T \\ 0 & 0 \end{bmatrix} \begin{Bmatrix} \hat{\theta}_D \\ \hat{D} \end{Bmatrix}_i}_{\text{control}} + \begin{bmatrix} T^2/2 \\ T \end{bmatrix} \omega_i$$

with  $Q = \langle \omega_i^2 \rangle$  from equation (18).

It remains to estimate the contribution of random-walk driving noise to the measurement  $(\theta_{CCD})_i$  in equation (11). The term should model the additional uncertainty in the measurement due to random fluctuations in drift since the previous measurement. If  $\omega_i$  is constant over any interval, the corresponding image position during the interval is  $-\theta_{D_i} - (t^2 \omega_i/2) - D_i t$  where  $t$  is measured from the beginning of the interval. The CCD averages the transient component resulting in:

$$\theta_{CCD_{i+1}} = -\theta_{D_i} - \frac{TD_i}{2} - \frac{T^2}{6} \omega_i \quad (19)$$

The dynamic equations for drift estimation (eq. (11)) become:

$$\begin{Bmatrix} \theta_D \\ D \\ \theta_{CCD} \end{Bmatrix}_{i+1} = \begin{bmatrix} 1 & T & 0 \\ 0 & 1 & 0 \\ -1 & -(T/2) & 0 \end{bmatrix} \begin{Bmatrix} \theta_D \\ D \\ \theta_{CCD} \end{Bmatrix}_i + \begin{Bmatrix} \text{control} \\ \text{term} \end{Bmatrix}_i + \begin{bmatrix} T^2/2 \\ T \\ -T^2/6 \end{bmatrix} \omega_i \quad (20)$$

### 3.4 Design of a Kalman Filter for Drift Estimation

The optimal estimation problem consists of equation (20) together with the measurement equation

$$y_{i+1} = (\theta_{CCD})_{i+1} + v_{i+1} \quad (21)$$

where  $v_{i+1}$  is the random noise in the CCD measurement; its expected rms value is given in figure 7.

The open-loop transition matrix for this problem is singular and noninvertible due to the fact that it contains a pure delay. However, the inverse is required for solution of the Euler Lagrange equations by eigenvector decomposition (ref. 11). Thus, this efficient numerical algorithm cannot be applied directly. The filter problem can be transformed, however, into one of reduced order to which eigenvector decomposition is applicable.

Equations (20) and (21) are replaced by the equivalent set

$$\begin{aligned} \begin{Bmatrix} \theta_D \\ D \end{Bmatrix}_{i+1} &= \begin{bmatrix} 1 & T \\ 0 & 1 \end{bmatrix} \begin{Bmatrix} \theta_D \\ D \end{Bmatrix}_i + \begin{bmatrix} -1 & -T \\ 0 & 0 \end{bmatrix} \begin{Bmatrix} \hat{\theta} \\ \hat{D} \end{Bmatrix}_i + \begin{bmatrix} T^2/2 \\ T \end{bmatrix} \omega_i \\ y_{i+1} &= [-1 \quad T/2] \begin{Bmatrix} \theta_D \\ D \end{Bmatrix}_{i+1} - [1/2 \quad T/2] \begin{Bmatrix} \hat{\theta} \\ \hat{D} \end{Bmatrix}_i - \frac{T^2}{6} \omega_i + v_{i+1} \\ &= [-1 \quad -T/2] \begin{Bmatrix} \theta_D \\ D \end{Bmatrix}_i + [1/2 \quad T/2] \begin{Bmatrix} \hat{\theta} \\ \hat{D} \end{Bmatrix}_i - \frac{T^2}{6} \omega_i + v_{i+1} \end{aligned} \quad (22)$$

The measurement noise is now correlated with the process noise:

$$\begin{aligned}
S &= \left\langle \left\{ \frac{T^2}{6} \omega_i + v_{i+1} \right\} \left\{ \omega_i \right\} \right\rangle \\
&= T^2/6 Q
\end{aligned} \tag{23}$$

An equivalent problem, in which the process noise and measurement noise are uncorrelated, is formed by adding an arbitrary multiple of the measurement equation (homogeneous form) to each state equation:

$$\begin{aligned}
\begin{Bmatrix} \theta_D \\ D \end{Bmatrix}_{i+1} &= \begin{bmatrix} 1 & T \\ 0 & 1 \end{bmatrix} \begin{Bmatrix} \theta_D \\ D \end{Bmatrix}_i + \begin{bmatrix} -1 & T \\ 0 & 0 \end{bmatrix} \begin{Bmatrix} \hat{\theta}_D \\ \hat{D} \end{Bmatrix}_i + \begin{bmatrix} T^2/2 \\ T \end{bmatrix} \omega_i \\
&+ \begin{bmatrix} L_1 \\ L_2 \end{bmatrix} \left\{ y_{i+1} + [1 \quad T/2] \begin{Bmatrix} \theta_D \\ D \end{Bmatrix}_i - [1/2 \quad T/2] \begin{Bmatrix} \hat{\theta}_D \\ \hat{D} \end{Bmatrix}_i + \frac{T^2}{6} \omega_i - v_{i+1} \right\}
\end{aligned}$$

Following the treatment of Bryson and Ho (ref. 12),  $L_1, L_2$  are determined so that the modified process noise and measurement noise will be uncorrelated:

$$\begin{aligned}
&\left\langle \left\{ \begin{bmatrix} T^2/2 \\ T \end{bmatrix} \omega_i + \begin{bmatrix} L_1 \\ L_2 \end{bmatrix} \left\{ T^2/6 \omega_i - v_{i+1} \right\} \right\} \left\{ -T^2/6 \omega_i + v_{i+1} \right\} \right\rangle \\
&= - \begin{bmatrix} T^4/12 \\ T^3/6 \end{bmatrix} Q - \begin{bmatrix} L_1 \\ L_2 \end{bmatrix} \left( \frac{T^4}{36} Q + R \right) = 0
\end{aligned}$$

where

$$R = \langle v_{i+1}^2 \rangle \Rightarrow \begin{bmatrix} L_1 \\ L_2 \end{bmatrix} = \left( \frac{-T^3 Q / R}{(T^4 / 36) Q + R} \right) \begin{bmatrix} T/2 \\ 1 \end{bmatrix} \tag{24}$$

Ignoring the measurement and control inputs to the state equations, an equivalent estimation problem can be defined by

$$\begin{aligned}
\begin{Bmatrix} \theta_D \\ D \end{Bmatrix}_{i+1} &= \begin{bmatrix} 1 + L_1 & T(1 + L_1/2) \\ L_2 & 1 + TL_2/2 \end{bmatrix} \begin{Bmatrix} \theta_D \\ D \end{Bmatrix}_i + \begin{Bmatrix} \omega_1 \\ \omega_2 \end{Bmatrix}_i \\
y_{i+1} &= [-1 \quad T/2] \begin{Bmatrix} \theta_D \\ D \end{Bmatrix}_{i+1} + v'_{i+1}
\end{aligned} \tag{25}$$

Measurement and process noise covariances for the equivalent problem are defined by

$$\begin{aligned}\left\langle \begin{Bmatrix} \omega_1 \\ \omega_2 \end{Bmatrix}_i \begin{bmatrix} \omega_1 & \omega_2 \end{bmatrix}_i \right\rangle &= \begin{bmatrix} T^2/4 & T/2 \\ T/2 & 1 \end{bmatrix} \left( 1 - \frac{T^4 Q/36}{(T^4/36)Q + R} \right) T^2 Q \\ \left\langle \begin{Bmatrix} \omega_1 \\ \omega_2 \end{Bmatrix}_i v'_{i+1} \right\rangle &= 0 \\ \langle (v'_{i+1})^2 \rangle &= \frac{T^4}{36} Q + R\end{aligned}$$

where

$$\begin{Bmatrix} \omega_1 \\ \omega_2 \end{Bmatrix}_i = \left[ \begin{bmatrix} T^2/2 \\ T \end{bmatrix} \omega_i + \begin{bmatrix} L_1 \\ L_2 \end{bmatrix} \left\{ T^2/6 \omega_i - v_{i+1} \right\} \right]$$

The problem in the form of equations (25) is solved by eigenvector decomposition (DISC program (ref. 11)) to obtain the optimal steady-state gains  $\begin{bmatrix} K_1 \\ K_2 \end{bmatrix}$ . The filter is implemented by reintroducing the measurement and control input terms in the estimate equations:

$$\begin{Bmatrix} \hat{\theta}_D \\ \hat{D} \end{Bmatrix}_{i+1} = \begin{Bmatrix} \bar{\theta}_D \\ \bar{D} \end{Bmatrix}_{i+1} + \begin{bmatrix} K_1 \\ K_2 \end{bmatrix} \left\{ v_{i+1} + \begin{bmatrix} 1/2 & 0 \end{bmatrix} \right\} \begin{Bmatrix} \hat{\theta}_D \\ \hat{D} \end{Bmatrix}_i$$

and

$$\begin{Bmatrix} \bar{\theta}_D \\ \bar{D} \end{Bmatrix}_{i+1} = \begin{bmatrix} L_1/2 & 0 \\ L_2/2 & 1 \end{bmatrix} \begin{Bmatrix} \hat{\theta}_D \\ \hat{D} \end{Bmatrix}_i + \begin{bmatrix} L_1 \\ L_2 \end{bmatrix} (v_{i+1}) \quad (26)$$

which yield

$$\begin{Bmatrix} \hat{\theta}_D \\ \hat{D} \end{Bmatrix}_{i+1} = \begin{bmatrix} L_1/2 + K_1/2 & 0 \\ L_2/2 + K_2/2 & 1 \end{bmatrix} \begin{Bmatrix} \hat{\theta}_D \\ \hat{D} \end{Bmatrix}_i + \begin{bmatrix} K_1 + L_1 \\ K_2 + L_2 \end{bmatrix} (v_{i+1}) \quad (27)$$

The  $z$  transform of the optimal discrete compensator follows from equation (27) and the control law  $\hat{\theta}_C_i = \hat{\theta}_D_i/T + \hat{D}_i$ :

$$\frac{\dot{\theta}_C(z)}{y(z)} = \frac{\left\{ \frac{(K_1 + L_1)}{T} + (K_2 + L_2) \right\} z - \frac{K_1 + L_1}{T}}{\left( z - \frac{L_1 + K_1}{2} \right) (z - 1)}. \quad (28)$$

The optimal filter has the same form as the compensation equation (14) which results from the standard estimate equations (12).

#### IV. PERFORMANCE OF THE IMAGE-MOTION COMPENSATION SYSTEM

In this section we exercise the analytical models, partially with linear analysis tools and partially by numerical simulation, to arrive at performance estimates of the system.

All performance estimates are based on the preliminary SIRTF geometric and dynamic data contained in figure 8. The section is organized into short-term and long-term analyses because the techniques used to perform each type of analysis tend to be similar.

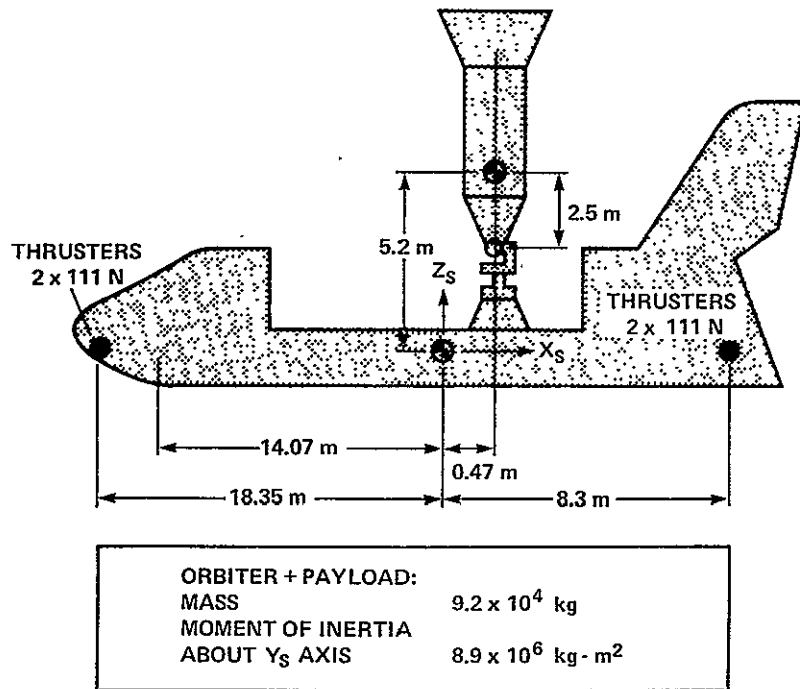


Figure 8.— Shuttle-SIRTF geometry (ref. 13).

#### 4.1 Short-Term Performance

All but the frequency response results in this section were obtained by the use of a numerical evaluation of the continuous dynamic equations (1) through (5) and the direct propagation of the discrete equations (11). This simulation approach focuses on the response of the system in periods between the updates provided by the CCD measurements. The frequency-response results were obtained by direct evaluation of the transfer functions contained in equations (6).

Figure 8 shows the nominal position of the telescope for a single-axis simulation about the Shuttle pitch axis. The angles of the elevation, cross elevation, and azimuth gimbals are zero.

The steady-state response of the gyro output  $\theta_g$  to a constant rate input  $\dot{\theta}_c$ , is zero because of the loop integrations; therefore, telescope attitude  $\theta$  drifts in the opposite sense of any gyro drift so as to null  $\theta_g$ . The transient response of  $\theta$  reflects the IPS bandwidth and  $\theta_g$  is equal to the transient deviation of  $\theta$  from its commanded value. Feed-forward of  $\theta_g$  to the image steering mirror removes IPS transients from the CCD image position to within the assumed feed-forward scale error. For purposes of this work, the scale-factor error has been assumed to be 5%.

Figure 9 shows the interaction in the frequency domain of the image-motion compensation and the 50 rad/sec telescope bending mode. The image response to inputs falls off slightly around the IPS bandwidth frequency. Figure 10 shows the significant effect of the feed-forward gain accuracy on the image response. Figure 11 shows similar responses to pivot accelerations. In all cases, the telescope and image motion track one another at frequencies below the IPS bandwidth, thus causing the gyro gimbal angle to be very small. As the IPS bandwidth is reached, the telescope ceases to respond, causing the gyro gimbal angle to increase; this gimbal angle error signal is used to command the mirror and maintain the image position at approximately the desired value. Although the bending effect produces some error, the perfect scale factor case in figure 10 shows that within the range of interest this error is very small.

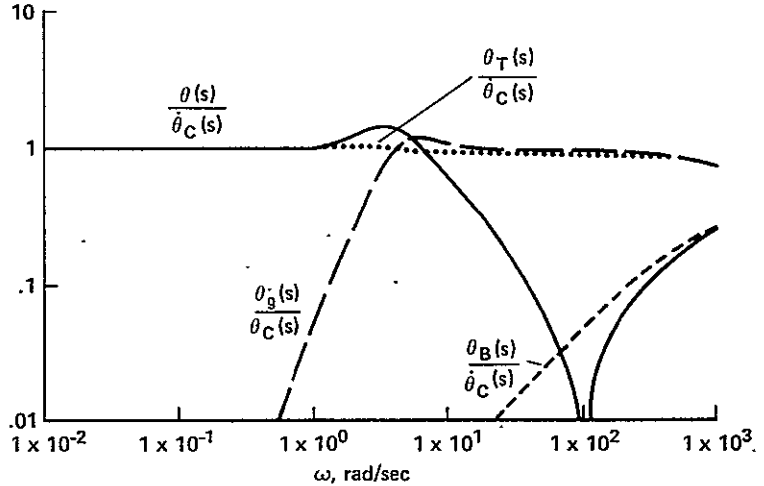


Figure 9.— Magnitude-frequency response of image position to commanded attitude,  $\theta_c$  (5% feed-forward scale error, 50 rad/sec bending mode).

Figure 12 illustrates two Shuttle disturbance inputs: an astronaut push-off and the Shuttle pitch control limit cycle. The limit cycle consists of  $\pm 0.1^\circ$  in attitude and  $\pm 0.01^\circ/\text{sec}$  in rate (ref. 13). The Shuttle accelerations of the gimbal torque the payload, whose center of mass is offset from the gimbal.

In the case of a rigid payload, the image position responds with the IPS elevation gimbal in proportion to the gyro feed-forward scale error. The telescope bending excited by the Shuttle

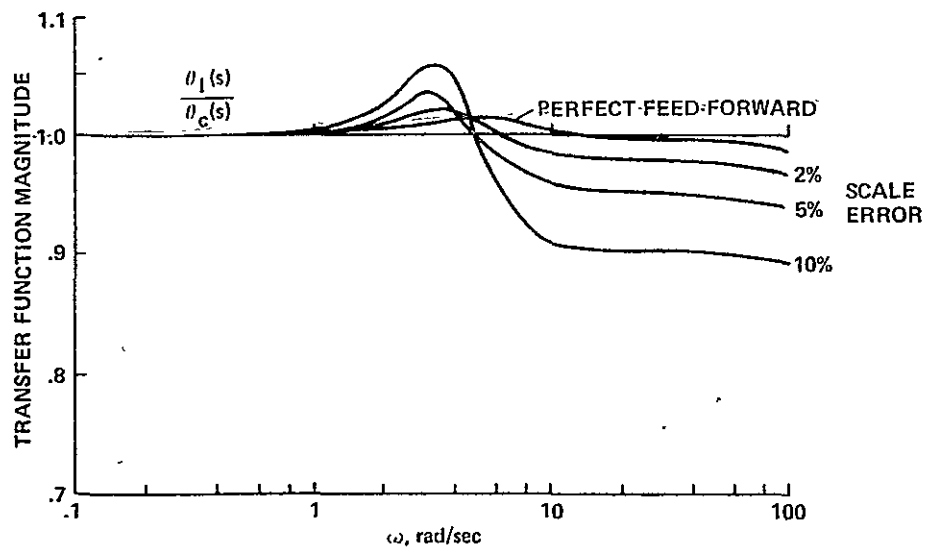


Figure 10.— Magnitude-frequency response of image position to pointing commands (effect of feed-forward scale error in the presence of a 50 rad/sec telescope bending mode).

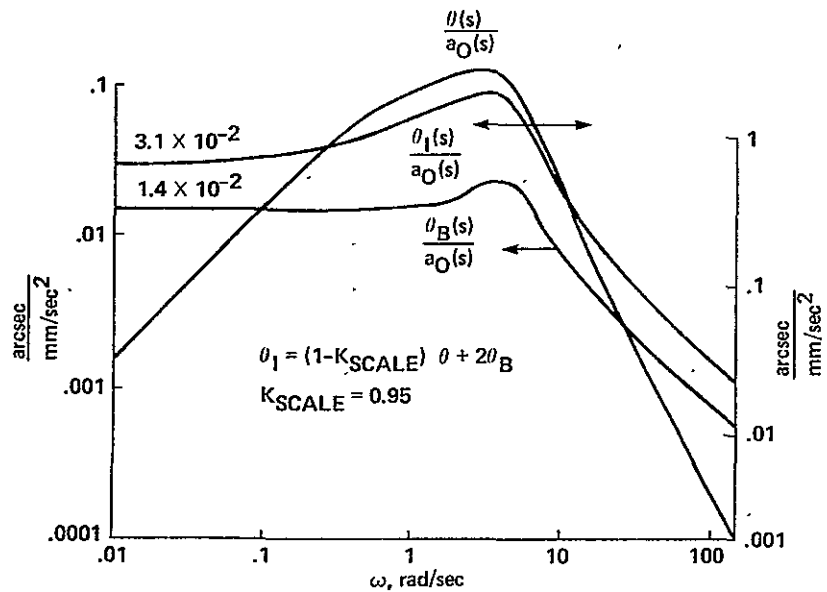
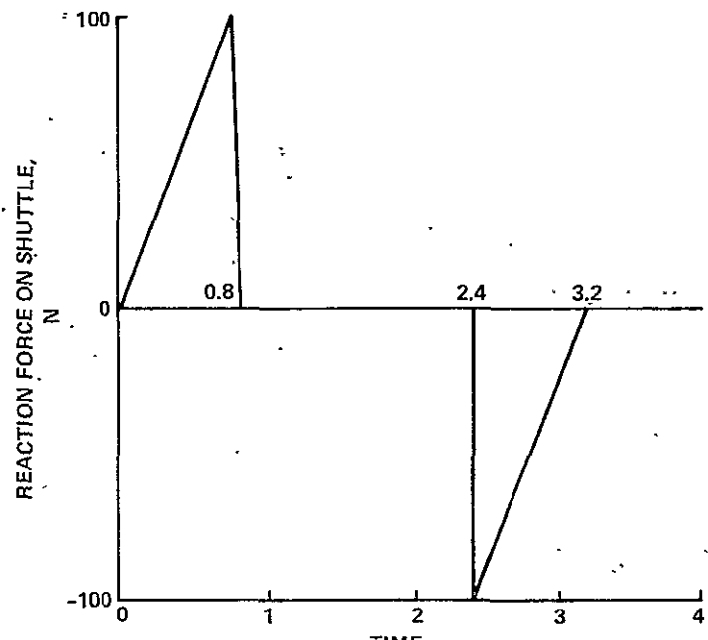
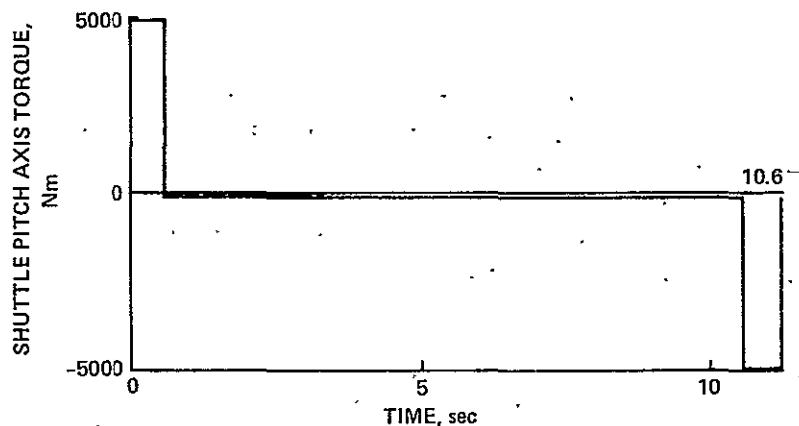


Figure 11.— Magnitude-frequency response of image position to acceleration  $a_0$  of telescope pivot along Shuttle roll axis.



(a) ASTRONAUT WALL PUSH-OFF



(b) SHUTTLE PITCH ATTITUDE LIMIT CYCLE

Figure 12.— Shuttle disturbances.

disturbance creates an additional component of image-position response equal to twice the bending angle. The telescope bending response limits the pointing accuracy that can be obtained in response to disturbances, regardless of how accurately the gyro feed-forward is scaled.

Figure 13 shows the image-position response  $\theta_I$  and the bending contribution  $\theta_B$  resulting from an astronaut push-off. These responses are derived by numerical integration of the continuous differential equations (1) to (5). For the 5% feed-forward scale error assumed, the image response does not exceed 0.1 arcsec. The bending contribution is about 30%; the remainder represents the residual of elevation gimbal response  $\theta$ , which can be reduced by more accurate feed-forward

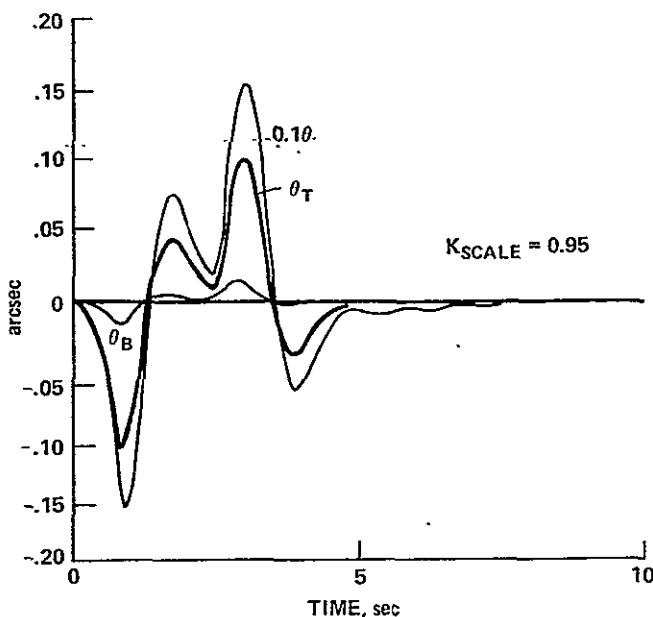


Figure 13.— IMC system response to astronaut wall push-off.

no with the star-tracker measurement sample times so that the drift estimator response is excited at a beat frequency that is the difference between the limit cycle frequency and the star-tracker sample rate.

Figure 14 shows the model used to derive the pointing response to the attitude limit cycle. The response of the high-sample-rate IPS control loop (herein referred to as the "continuous loop") and the payload bending excitation are calculated by numerical integration of the differential equations (1) to (5), as in the case of the astronaut push-off. A fourth-order Runge Kutta algorithm and time step of 0.02 sec were used for this purpose. The peak image position response in figure 15(a) exceeds 0.2 arcsec with a 30% contribution from bending. Once again, no IPS accelerometer feed-forward is assumed.

Although a small integration step size is necessary because of the high-frequency payload bending dynamics, an inordinate amount of computation would be required to generate the digital control-loop excitation occurring in response to the attitude-limit cycle over relatively long periods of time. Numerical integration is avoided in this case by means of an analysis using a state transition matrix and inverse Laplace transformation.

Figure 15(b) shows the image-position response to the digital filter outputs induced by the attitude-limit cycle. The filter outputs are in response to the combination of the two image responses shown in figure 14. These responses are shown separately to emphasize the large difference in magnitude and time scale between the continuous- and discrete-loop responses.

The discrete-loop response is for a 14th magnitude star filter at a 21-sec integration time. This is the sample time that minimizes the drift pointing error for the Ferranti gyro (table 1). The limit cycle period is 21.2 sec so that two counteracting disturbances occur every filter sample period. The star-tracker measurement is not strongly excited as a result, and the discrete control activity is not

scaling. It should be noted that the  $\theta$  response shown is for the case where there is no feed-forward of the IPS accelerometer measurement. In actuality the feed-forward of the IPS base accelerations to the gimbal torquers will directly improve the accuracy of the IMC alone by reducing both the IPS and bending responses.

The other short-term disturbance considered is the action of the vernier reaction control system for the Shuttle pitch attitude. The Shuttle torque profile of figure 12 produces accelerations of the elevation gimbal along the Shuttle roll axis of  $1.8 \text{ mm/sec}^2$  and of 0.6-sec duration. The accelerations, which occur in alternating directions every 10.6 sec, periodically excite short-term responses of both the IPS and the payload bending mode. The resulting periodic disturbance of the star-tracker image is asynchronous

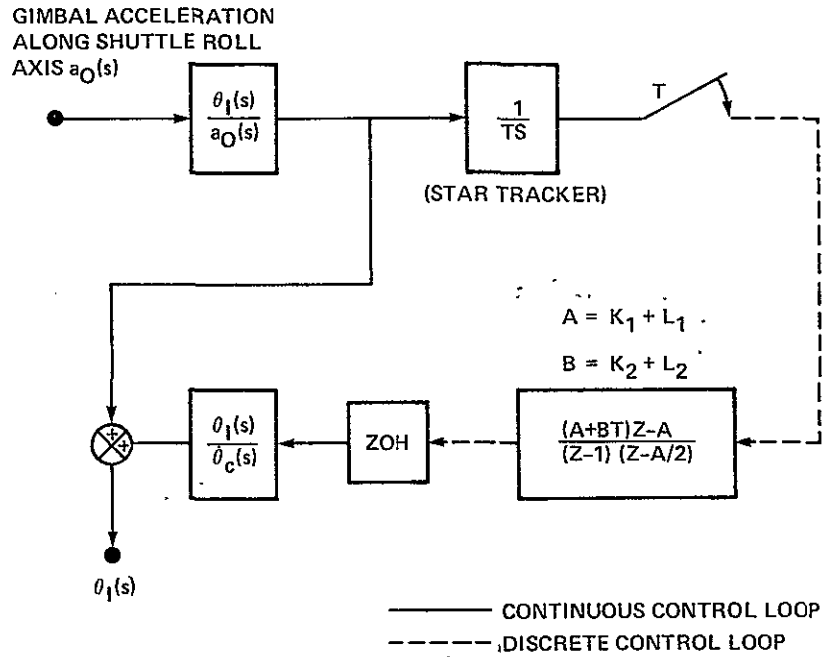


Figure 14.— Simulation model for response to Shuttle limit cycle.

significant in the total image motion. At shorter sample times the star tracker will measure individual thruster disturbances and the discrete-loop response will be larger.

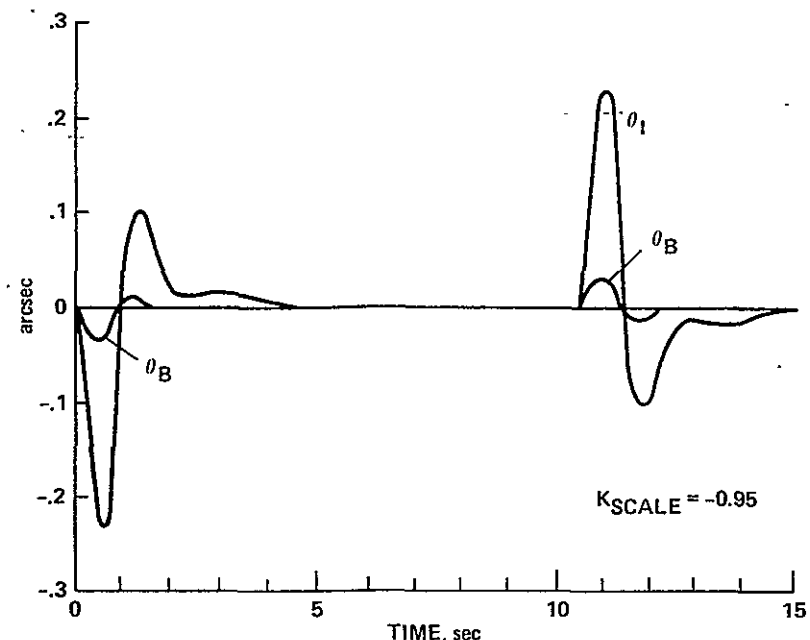
#### 4.2 Long-Term Performance

Performance of the IMC system over a long term entails the use of a numerical simulation for the cases involving slow transients and the use of linear system covariance analysis for the cases involving steady-state response to system noise.

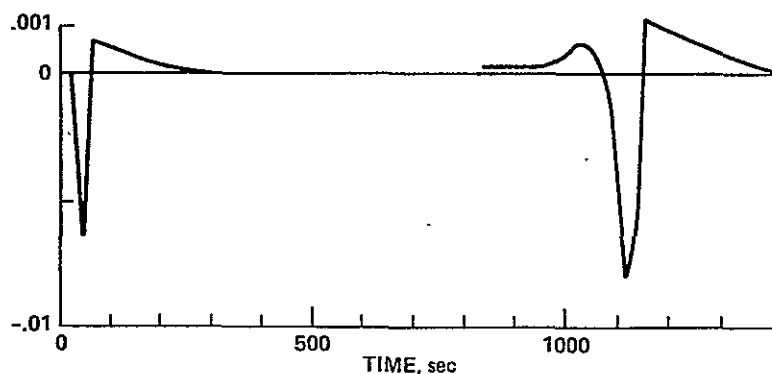
*4.2.1 Simulation description*— The long-term simulation determines the performance of the digital drift filter and the response to pointing disturbances that are observable by the star tracker. These include gyro drift, gyro feed-forward scale error, and mechanical and thermal strains.

In section 3, the star tracker was modeled over many sample periods by a transfer function of  $1/TS + 1$  (eq. (8b)). This transfer function is used in calculating the contribution of high-frequency gyro rate noise to the star-tracker measurement error, which is a discrete, purely random sequence that is uncorrelated with the intrinsic star-tracker sensor noise. Its rms magnitude is given as a function of the star-tracker integration time in figure 6. Figure 16 is the gyro rate noise model of the IMC system.

The purpose of separately modeling rate-noise effects is to eliminate the IPS and bending dynamics from the long-term simulation. This allows the integration step size to be large. Short-term responses show that bending and imperfect feed-forward do not significantly affect the response to gyro inputs. The two gyro inputs considered in the long-term simulation are random-walk



(a) IMAGE POSITION RESPONSE ARISING FROM 5% FEED-FORWARD SCALE ERROR AND TELESCOPE BENDING



(b) IMAGE POSITION RESPONSE TO DISCRETE CONTROL ACTION

Figure 15.— Response to Shuttle pitch-attitude limit cycle.

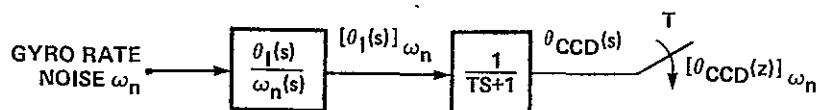


Figure 16.— Contribution of high-frequency gyro rate noise to star-tracker measurement.

drift and digital filter commands. Figure 17 shows the long-term simulation model. The image responds perfectly to gyro inputs in this model since feed-forward scale error and bending are neglected.

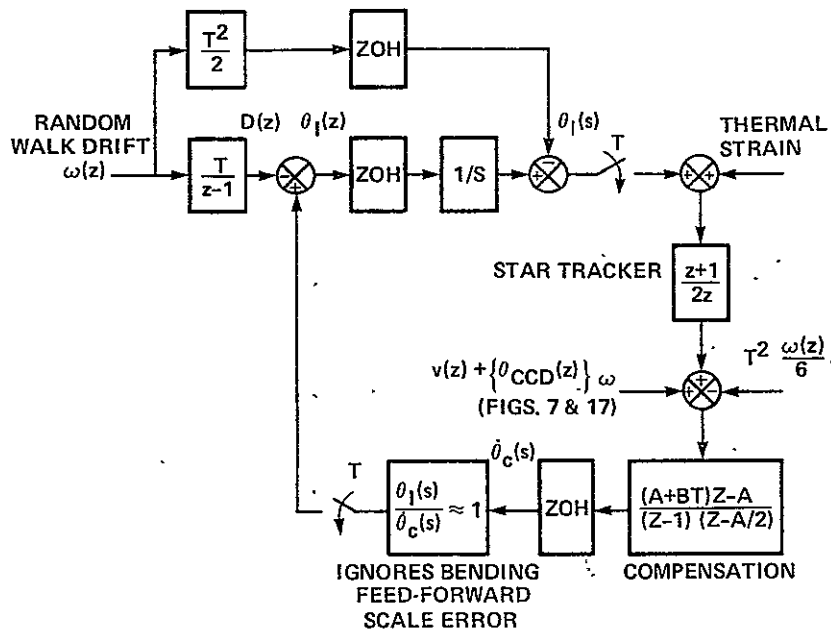


Figure 17.— Long-term response model of the image motion compensation system.

The digital control loop provides attitude rate commands that are the updates of the Kalman filter designed in section 3. These are maximum likelihood estimates of image position based on noisy star-tracker measurements. The image is disturbed by random-walk variations in drift. The charge coupled device (CCD) in the star tracker must integrate the incident starlight for an interval of time before outputting pixel signals. For each star of a different magnitude, a particular star-tracker integration time and sample period results in the best overall accuracy of drift estimates. The design integration sample time represents an optimum between favorable estimation accuracy for short sample times and favorable star-tracker measurement accuracy for long integration times. For the Ferranti model 125 gyro and a 14th magnitude star, the rms drift estimate error is 0.0093 arcsec/sec at an optimal sample time of 21 sec (table 2). The post update estimate error can be

TABLE 2.— OPTIMAL SAMPLE TIMES AND THE CORRESPONDING MINIMUM POINTING ERROR

Gyro	Steady pointing		Chopping		Image jitter arising from high-frequency gyro rate noise, arcsec rms
	Best sample time, sec	Minimum pointing error, arcsec rms	Best sample time, sec	Minimum pointing error, arcsec rms	
Hamilton Standard RI-1139	10	2.7×10 <sup>-2</sup>	12	4.2×10 <sup>-2</sup>	0.015
Bendix 64 PM and Ferranti 125	21	0.3×10 <sup>-3</sup>	25	1.4×10 <sup>-2</sup>	0.0068

further reduced at even longer integration times, but at sample times larger than 21 sec the closed-loop pointing error increases. The closed-loop pointing error is shown to be the prior update estimate accuracy in section 4.2.6.

The heart of the digital control simulation is the digital star-tracker simulation of reference 10. The star-tracker model is closely patterned after the actual device. Integration of the incident light intensity is carried out over each pixel and an independent time-random noise added to each pixel signal. The geometry of the image and the CCD array are accounted for. Star centroids are determined by the interpolation algorithm described in the appendix.

The actual image intensity distribution formed on the face of the CCD array with image motion is the convolution of the stationary intensity distribution. For the purpose of discrete simulation, the image motion is approximated by a uniform rate over each time step. In figure 18,  $I$  (photons/ $\mu\text{m}^2/\text{sec}$ ) is the instantaneous image intensity distribution;  $(y', z') = (y, z + Dt)$  define position on the CCD array relative to the initial image position; and  $(y, z)$  define position relative to the instantaneous image center, which is moving uniformly at a rate of  $D \mu\text{m/sec}$ . The integral with respect to time of the time-varying intensity at any point is equivalent to an integral with respect to position of the stationary intensity distribution

$$\int_0^t I(y', z', t) dt = \frac{1}{D} \int_{z' - Dt}^{z'} I(y, z) dz \quad (29)$$

The right-hand expression is used for calculating pixel signals in the simulation of the star tracker. Detailed information about the star tracker is given in reference 10.

It is quite expensive to integrate the image intensity distribution several times during each sample interval. If the image position rate is assumed to be constant over a filter sample period, the star-tracker measurement that is obtained by exact simulation is very nearly the average image position. In the simulation responses that follow, the star-tracker measurement is modeled as the average of the current image position and the image position at the previous sample time. This allows an order of magnitude reduction in computation time without adversely affecting accuracy. Averaging the image positions is equivalent to modeling the star tracker by the transfer function:

$$\frac{\theta_{CCD}(z)}{\theta_I(z)} = \frac{z+1}{2z}$$

which was discussed in section 3 (eq. (8)).

**4.2.2 Simulation results for transient response**— The star-tracker noise for a 14th magnitude star measurement is much higher than the Ferranti gyro drift noise. This results in small measurement feedback gains and a slow digital filter transient response. Figure 19 is the image position response for an initial error of -1 arcsec in  $\theta_g$  and -0.1 arcsec/sec in  $\dot{\theta}_g$ . The image position error increases to 6 arcsec before significant correction to the initial drift rate is provided by the filter. The position error returns to nearly zero in about 10 min.

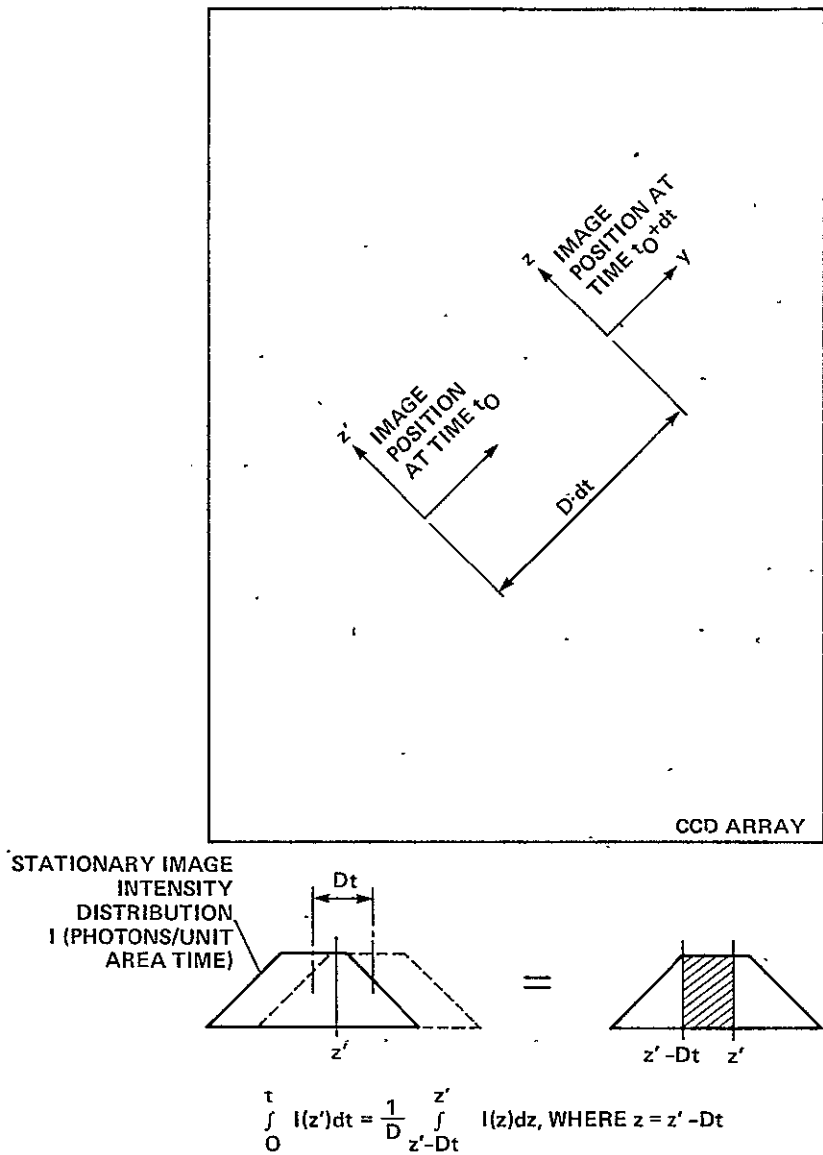


Figure 18.— Interpretation of intensity distribution resulting from uniform image motion as a convolution of the stationary intensity distribution.

To speed up the slow response to large deterministic image position biases, the filter gains have to be increased. In fact a “finite settling” design, which is unique to discrete systems, can null an arbitrary initial state in three sample periods (63 sec) in a highly oscillatory response. In a practical system, the finite settling gains could be employed whenever the image position error exceeds a predetermined level. The error will not be nulled exactly because the deterministic image position bias may be slowly changing; also, random sensor noise is present. The finite settling gains will give the best transient response until the response becomes dominated by the sensor noise. After that point, the Kalman filter gains are used because the high finite settling gains only magnify the already high measurement noise. A suitable error level for switching gains is 0.1 arcsec in the case of 14th magnitude star measurements.

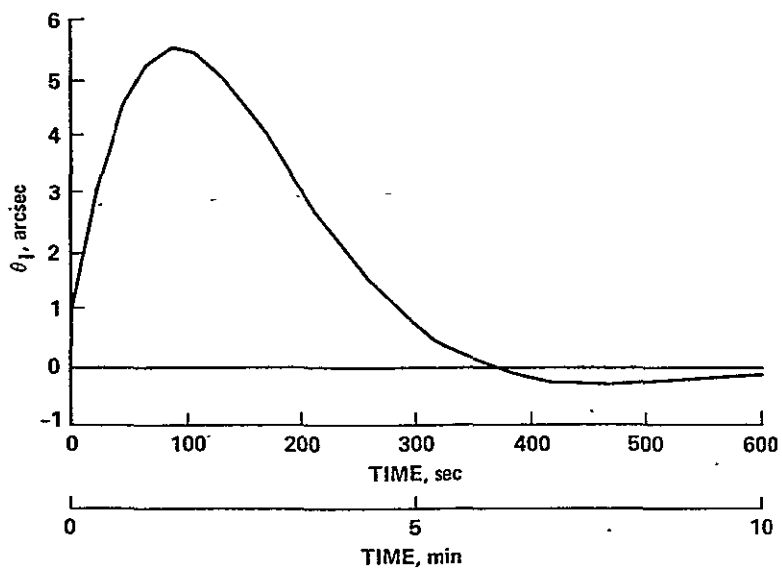


Figure 19.— Image position response to initial attitude error or -1 arcsec and constant drift rate of -0.1 arcsec/sec fine-pointing filter for 14th magnitude star (21-sec integration time).

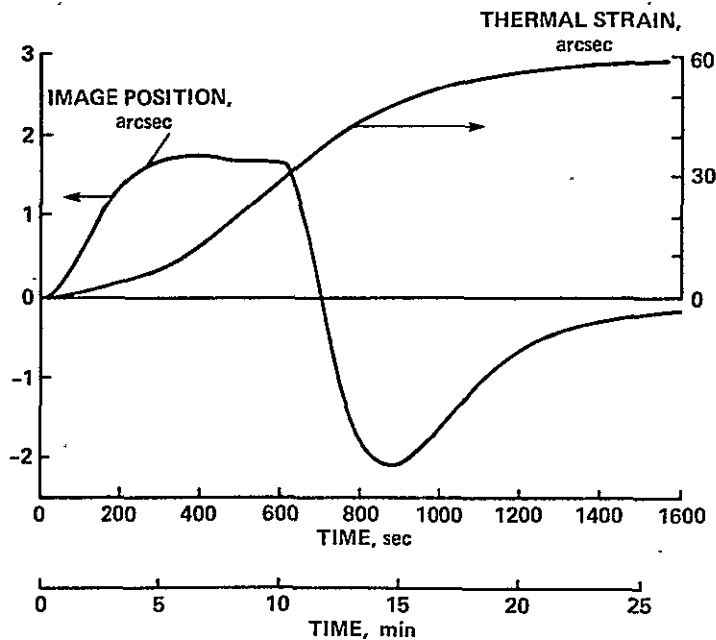


Figure 20.— Response to thermal strain with fine-pointing filter for 14th magnitude star (21-sec integration time).

**4.2.3 Simulation results for the thermal pointing disturbance—** Figure 20 shows a hypothetical pointing disturbance of the telescope that might be caused by a change of the solar illumination incident on the Shuttle. The thermal-strain transient is characterized by a continuous first derivative, that is, no discontinuities in strain rate. This type of pointing error is not observable by the gyros, which undergo no change in orientation. The disturbance of the image is measured by the star tracker, and the filter commands the telescope to an offset position that compensates for the thermal disturbances.

The image response in figure 20 is for the 14th magnitude star filter at a 21-sec sample time. The digital control is effective in reducing the 60-arcsec disturbance to a peak error of 2 arcsec.

**4.2.4 Simulation results for sensor noise—** The sensor noise inputs in the long-term simulation are shown in figure 17. The inputs correspond to the noise terms in equations (20) and (21). The IMC response is simulated for the  $T = 21$  sec, 14th magnitude star filter over a period of 2,000 samples, or 12 hr. The rms pointing error is  $9.3 \times 10^{-3}$  arcsec.

**4.2.5 Analytical drift estimate accuracy—** Optimal filters are designed using the analysis in section 3.4 for a worst-case 14th magnitude guide star. Star-tracker measurement error covariances are determined from figure 7, based on a 15-arcmin field of view and 50 photoelectron background noise level.

Figure 21 shows the influence of sample-integration time on the minimum variance drift estimate accuracy. Results are presented for both a Ferranti 125 gyro (comparable to Bendix 64 PM) and a Hamilton Standard RI-1139 gyro.

The telescope may be used in a mode where the steering mirror position is dithered with a square waveform or "chopped." This creates two star images, each having an intensity equal to 45% of the intensity developed in a steady image over an equivalent integration interval. The net integration time for a single image becomes 0.45 times the star-tracker sample time. The resulting increased measurement noise increases the drift estimate error as shown.

The drift estimate errors presented here are based on perfect centroid determination of the defocused star image on the CCD array. Errors of interpolation for chopped and steady images are discussed in the appendix. These errors are reduced to about 0.02 pixels, maximum, by use of an appropriate interpolation algorithm. This amounts to a static (non-time dependent) error of 0.06 arcsec in the case of a 15 arcmin field of view.

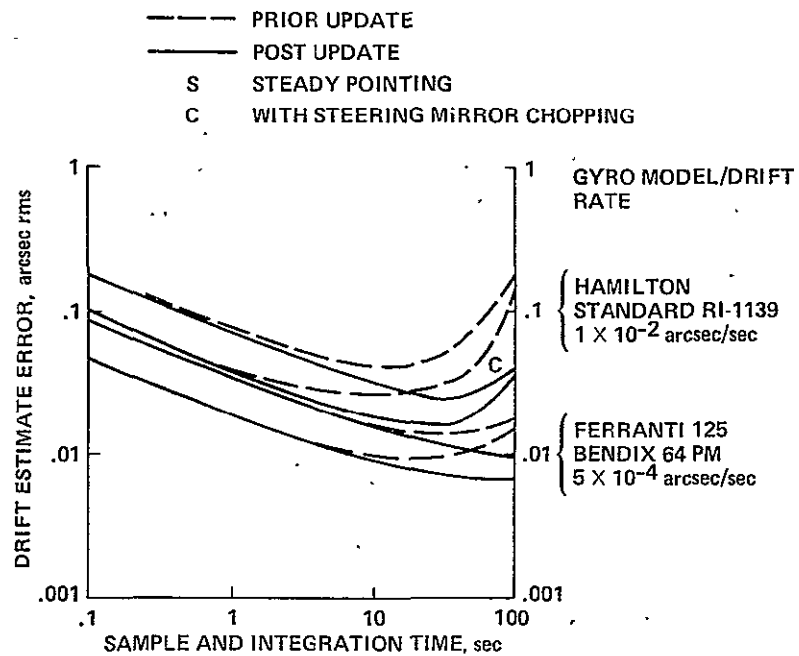


Figure 21.— Drift estimate error vs sample time for a 14th magnitude star.

**4.2.6 Analytical closed-loop pointing accuracy in the presence of drift**— The output of the gyro resulting from uncorrected random-walk drift is  $\theta_{D_{i+1}}$ . This is the uncorrected error in the image position in the focal plane, if there is no scale error in the feed-forward of gyro output to the image steering mirror. The rms pointing error is related to the post measurement update estimate errors by:

$$\begin{aligned}\theta_{D_{i+1}} &= \theta_{D_i} + D_i T - \hat{\theta}_{D_i} - \hat{D}_i T + \frac{T^2}{2} \omega_i \\ &= -\tilde{\theta}_{D_i} - T \tilde{D}_i + \frac{T^2}{2} \omega_i\end{aligned}$$

where

$$\tilde{\theta}_{D_i} \equiv \hat{\theta}_{D_i} - \theta_{D_i}$$

$$\tilde{D}_i \equiv D_i - \bar{D}_i$$

and

$$\langle \theta_{D_{i+1}}^2 \rangle = \langle \tilde{\theta}_{D_i}^2 \rangle + 2T\langle \tilde{\theta}_{D_i} \cdot \tilde{D}_i \rangle + \langle \tilde{D}_i^2 \rangle + \frac{T^4}{4} Q$$

This is precisely the pre-update estimate error. Thus, the pre-update error curves of figure 21 also give the closed-loop pointing error in the presence of drift.

As can be seen from figure 21, there is an optimum sample time that yields the minimum pointing error. This choice of sample time results in the best trade-off between sensor and process noise. The pointing error remains well within the 0.1-arcsec requirement over a wide range of sample times.

Table 2 summarizes the optimum integration times for the four cases presented and also gives the resulting pointing error for that sample time. It is worthwhile to note that the pointing error of 0.0093 arcsec shown for the steady error with the Ferranti gyro was also predicted by the long-term simulation results described in section 4.2.4. This provides a verification on these two substantially different methods of arriving at the results.

## V. CONCLUSIONS

The performance of an image-motion compensation (IMC) system for The Shuttle Infrared Telescope Facility, which uses a focal plane CCD star tracker and a steerable mirror, has been analyzed for motion in one axis. The IMC system is necessary because the stringent pointing requirements (0.1 arcsec) for SIRTF cannot be met by the Shuttle-mounted instrument pointing system (IPS). Use of the CCD at the SIRTF focal plane provides gyro offset and drift correction and facilitates a star-field display for the SIRTF operator.

Results of the analysis show that the steady-state jitter due to gyro and CCD noise is less than 0.02 arcsec for the faintest stars to be used (14th magnitude). This performance can be achieved for steady pointing and while chopping. It assumes that a gyro is used with drift performance equal to that of the Ferranti or Bendix 64 PM for the IPS. Furthermore, these pointing stabilities are achieved with CCD integration times between 4 and 100 sec, with the best results (0.01 arcsec) at a 21-sec integration time.

To obtain the results given above, the CCD error model was exercised for both the steady pointing and the chopping case. The interpolation error, which was essentially unchanged by the chopping, was approximately 0.06 arcsec (with a 15-arcmin field of view) for both cases. However,

due to the fainter image while chopping, the total CCD error was approximately doubled for this case.

Results of the transient analysis show that the IMC system attenuates many of the shuttle disturbances on focal plane image motion. Specifically, an astronaut wall push-off produces a maximum image-motion excursion of 0.1 arcsec for a feed-forward scale-factor error of 5%. Shuttle attitude-control limit cycles produce an image motion of  $\pm 0.23$  arcsec for a scale-factor error of 5%. An 8-Hz bending mode was included in this analysis and accounts for about 30% of these transient errors. The remainder, due to the scale-factor error, can be reduced by improving the scale-factor accuracy. This analysis assumes there is no accelerometer feed-forward incorporated in the IPS. In fact, this improvement in the IPS will likely be incorporated. Therefore, to reduce image motion during Shuttle limit cycles to less than 0.1 arcsec, either the gyro-mirror feed-forward scale factor has to be accurate to 1%, or the combination (product) of the IPS accelerometer feed-forward scale factor and the gyro-mirror scale factor has to be accurate to 1%; the latter accuracy should be easily achievable.

Although a simple bending model was chosen for the analyses above, its frequency (8 Hz) was selected to be lower than will likely be the case in the final design; therefore, its effect is likely larger than will ultimately be the case. With this conservative assumption, bending was found to have no effect on steady-state jitter and only the small effect on the transient response discussed above.

## APPENDIX A

### STAR-TRACKER INTERPOLATION ERROR

The face of the CCD detector is divided into a rectilinear pattern of discrete photosensitive elements. Each element integrates the incident light intensity by the accumulation of the photoelectrons that are excited. The location of each photosensitive element is uniquely specified so that it is possible to obtain the precise coordinates within the resolution of the element array of any stars being imaged on the surface of the CCD. The state of the art for CCD's is an array of 800 elements square. Thus, even the most advanced units cannot obtain resolution better than 1.1 arcsec for a 15-arcmin field of view.

It is possible, through a process of interpolation, to extend the resolution by more than an order of magnitude. The star image is defocused into an intensity distribution over a four-by-four matrix of elements. The center of charge is then computed, which results in an image centroid location within an individual pixel.

State errors of interpolated star positions interact strongly with the shape of the defocused image. As a defocused image moves around on the array, the error of the interpolated image center and the total signal level fluctuate. These effects are largely caused by the opaque registers, which in the Fairchild 211 CCD are columns of photosensitive elements. The image shape and size can be adjusted to control total signal modulation, calculation sensitivity to pixel noise, and the centroid error.

The SIRTF focal plane guidance sensor design is unsettled at this time so the Zenith catadioptric optics of the Ames Video Inertial Pointing System are used as a representative optical design (ref. 14). A study by Marx at the Jet Propulsion Laboratory (ref. 15) shows that a four-element interpolation algorithm coupled with an image width of 2.75 horizontal pixel units results in the following favorable measurement characteristics:

1. Total signal modulation, 1.5%
2. Minimum collected signal, 40%
3. Worst-case sensitivity to pixel noise, 0.11 elements
4. Centroid error, 0.06 elements.

A digital computer simulation of the CCD is used to predict interpolation errors. The characteristics of the assumed image intensity distribution conform to the recommendations of reference 15. The assumed image shape, shown in figure 22, is trapezoidal and covers 2.75 pixels in the horizontal direction. Its line spread is formed by integrating the two-dimensional image intensity distribution in one dimension. The line spread for the image assumed in the simulation roughly corresponds to the experimental line spread for a similar size image of the Zenith optics (ref. 16), as shown in figure 23.

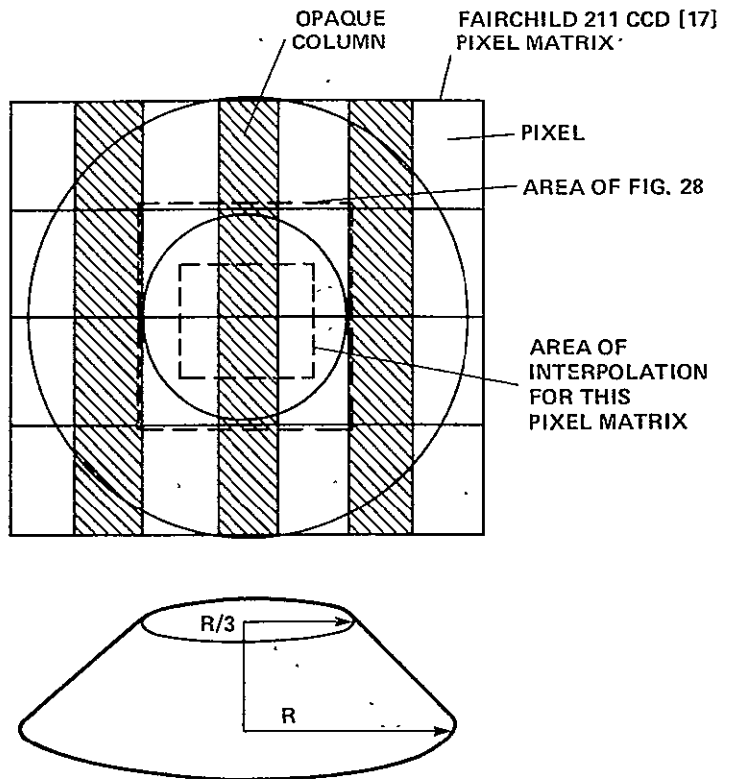


Figure 22.— Assumed defocused star image: shape and size relative to CCD pixel matrix.

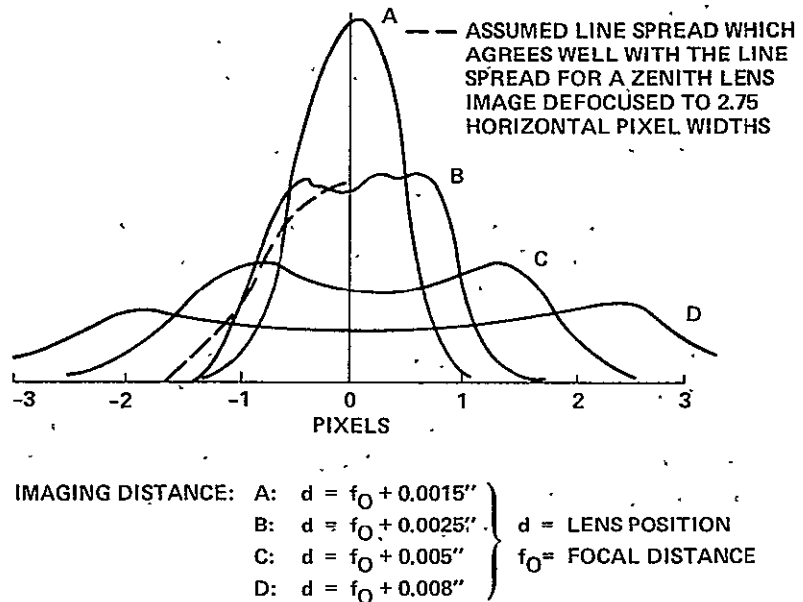


Figure 23.— Comparison of line spreads for a zenith catadioptric lens with glass plate with line spread for defocused image of figure 22.

In the simple center-of-charge interpolation algorithm, the pixel signals  $S_{ij}$  are summed row-wise and column-wise to form vertical and horizontal line spreads  $S_i$  and  $S_j$ :

$$S_i = \sum_{j=1}^4 S_{ij}$$

$$S_j = \sum_{i=1}^4 S_{ij}$$

The centroid address in pixels is

$$\hat{k} = \frac{1.5(S_4 - S_1) + 0.5(S_3 - S_2)}{S}$$

relative to the matrix center where

$$S = \sum_{i=1}^4 S_i = \sum_{j=1}^4 S_j$$

The above formula is exact only for a uniform intensity line spread and for a CCD with no opaque registers. For the nonuniform distribution in figure 22, the Fairchild 211 CCD physical layout, the following approximate corrections give almost an order of magnitude increase in accuracy:

$$\hat{k}_{\text{vertical}} \leftarrow 1.3193 \hat{k}_{\text{vertical}}$$

$$\hat{k}_{\text{horizontal}} \leftarrow \pm(-0.7024 + \sqrt{0.4933 + 1.905|k_{\text{horizontal}}|})$$

This interpolation algorithm can also be used while the steering mirror is chopping. In the chop mode there are two defocused star images, each with 45% of the intensity of a single image. The two images are connected by a faint, streaked image along which 10% of the incident intensity is distributed. The intensity of the streaked image is determined from the angular separation of the stationary images, which is assumed to be 5 arcmin.

Figures 24 and 25 show the stationary and streaked images, respectively. The intensity of the streaked image is about two orders of magnitude less than that of the stationary image. The effect of the tail on the stationary image interpolation is therefore quite small. Figure 26 shows the interpolation errors in pixel units for both chopping and steady pointing and their dependence on image centroid position. The maximum centroid error of 0.017 pixels corresponds to 0.06 arcsec in a 15-arcmin field of view. The same interpolation algorithm is used for chopped and stationary images.

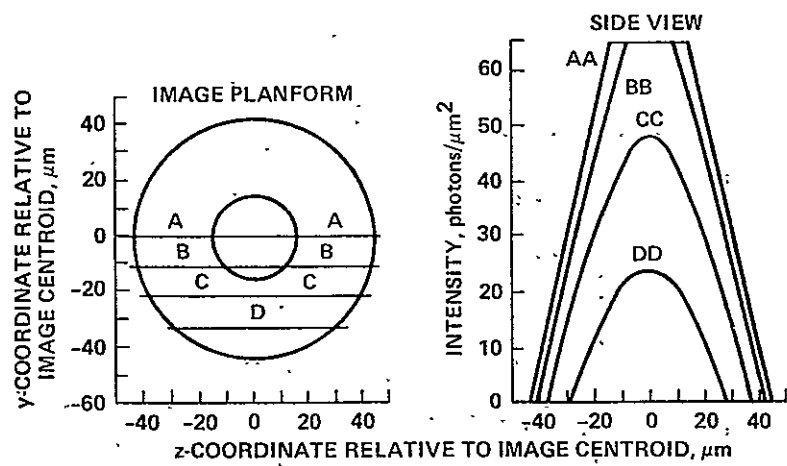


Figure 24.— Defocused star image during 5-arcmin square wave chopping (10-sec integration time, 14th magnitude star).

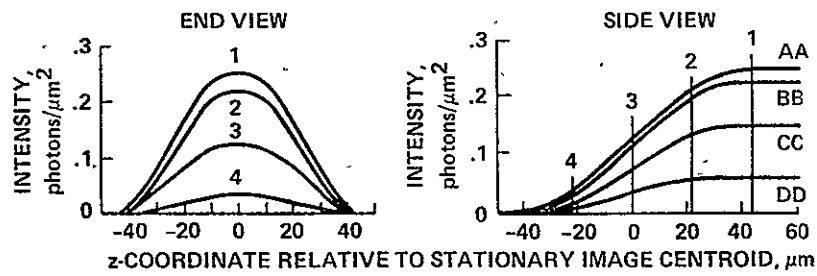
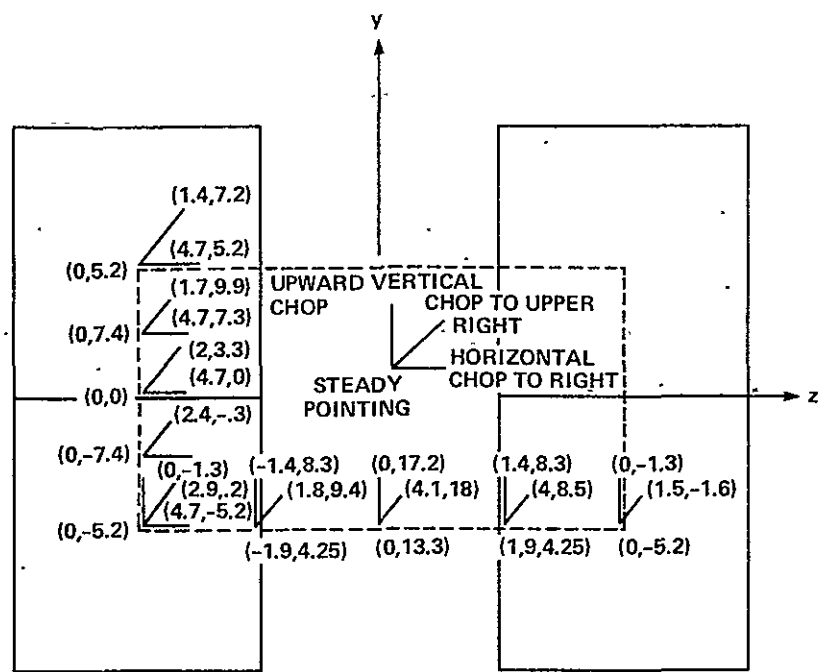


Figure 25.— Scanned image shape during 5-arcmin square wave chop to right.



( $dz, dy$ ) INTERPOLATION ERRORS IN HORIZONTAL AND VERTICAL DIRECTIONS RESPECTIVELY (IN UNITS OF  $10^{-3}$  PIXELS)

Figure 26.— Interpolation errors with and without chopping.

## REFERENCES

1. Fazio, G. G.: IR Astronomy Zooms to Prominence. *Astronaut. and Aeronaut.*, vol. 5, 1978, pp. 40-51.
2. Lee, G. K.: Video Inertial Pointing System Software Documentation. Technical Note 1335-53-04, Informatics, Inc., Palo Alto, Calif., 1978, pp. 27-29.
3. Lorell, K. R.; Murphy, J. P.; and Swift, C. D.: A Computer-Aided Telescope Pointing System Utilizing a Video Star Tracker. VII IFAC Symposium on Automatic Control in Space, Rottach-Egern, Federal Republic of Germany, May, 1976.
4. McCarthy, S. G.: Shuttle Infrared Telescope Facility Preliminary Design Study. Final Report, Hughes Aircraft Co., Culver City, Calif., 1976, pp. 3-59-3-98.
5. Murphy, J. P.; Lorell, K. R.; and Swift, C. D.: A Computer-Aided Telescope Pointing System Utilizing a Video Star Tracker. NASA TM X-73,079, 1975, pp. 12-14.
6. Powell, J. D.; and Throckmorton, A. J.: A Study of Filter Mechanizations for the Video Inertial Pointing System Microprocessor. Final Report, Guidance and Control Laboratory, Department of Aeronautics and Astronautics, Stanford University, Stanford, Calif., 1975.
7. Salomon, P. M.; and Goss, W. C.: A Microprocessor-Controlled CCD Star Tracker. 14th Aerospace Sciences Meeting, AIAA, Washington, D.C., Jan. 1976.
8. Witteborn, F. C.; and Young, L. S.: A Cooled Infrared Telescope for the Space Shuttle — the Shuttle Infrared Telescope Facility (SIRTF). AIAA Paper 76-174, 21st Annual Meeting of the Amer. Astronaut. Soc., Denver, Aug. 1975.
9. Young, L. S.; Witteborn, F. C.; and Kiya, M. K.: Shuttle Infrared Telescope Facility Interim Report. Appendix B3, Ames Research Center, NASA, Moffett Field, Calif., 1978.
10. Powell, J. D.; and Parsons, E. K.: Control System Concepts for the Shuttle Infrared Telescope Facility. SUDAAR Report No. 510, Guidance and Control Laboratory, Department of Aeronautics and Astronautics, Stanford University, Stanford, Calif., 1978.
11. Katz, P.; and Powell, J. D.: Selection of Sampling Rate for Digital Control of Aircraft. SUDAAR Report No. 486, Guidance and Control Laboratory, Department of Aeronautics and Astronautics, Stanford University, Stanford, Calif., 1974.
12. Bryson, A. E.; and Ho, Y. C.: *Applied Optimal Control*. Hemisphere Publishing Corp., Washington, D.C., 1975.
13. Dornier System Document, IPS-DS-TN-0094.
14. Final Report 760-175 for Flight Demonstration Model Star Sensor, Jet Propulsion Laboratory, Pasadena, Calif., 1977.
15. Marx, H. B.: Optimal Coupling of Star Image Characteristics with Algorithm Form for an Accurate Inter-Element Star Position Determination. Memorandum 343-8-75-510, Jet Propulsion Laboratory, Pasadena, Calif., 1975.

16. Marx, H. B.: Image Characteristics of the Zenith 130 mm Catadioptric Lens as Affected by Defocus and Lens-Temperature. Memorandum 343-8-75-732, Jet Propulsion Laboratory, Pasadena, Calif., 1975.
17. Fairchild CCD 211 Preliminary Data Sheet, Mar. 1976.

1 Report No NASA TM-81159	2 Government Accession No.	3. Recipient's Catalog No	
4 Title and Subtitle  CONTROL SYSTEM DESIGNS FOR THE SHUTTLE INFRARED TELESCOPE FACILITY		5 Report Date	
7 Author(s) J. David Powell* and Eric K. Parsons* and Kenneth R. Lorell**		6. Performing Organization Code	
9 Performing Organization Name and Address *Department of Aeronautics and Astronautics, Stanford University, Stanford, Calif. 94305 **Ames Research Center, NASA, Moffett Field, Calif. 94035		8. Performing Organization Report No. A-8018	
12. Sponsoring Agency Name and Address National Aeronautics and Space Administration Washington, D.C. 20546		10. Work Unit No. 358-41-06	
15. Supplementary Notes		11. Contract or Grant No.	
		13 Type of Report and Period Covered Technical Memorandum	
		14. Sponsoring Agency Code	
16 Abstract  The Shuttle Infrared Telescopy Facility (SIRTF) is being designed as a 0.85-m, cryogenically cooled telescope capable of a thirtyfold improvement over currently available infrared instruments. The SIRTF, mounted in the Orbiter on the Instrument Pointing System (IPS), requires that the image at the focal plane be stabilized to better than 0.1 arcsec with an absolute accuracy of 1 arcsec in order to attain this goal. Current estimates of IPS performance for both stability and accuracy indicate that additional stabilization will be necessary to meet the SIRTF requirements. An Image Motion Compensation (IMC) system, utilizing a Charge Coupled Device (CCD) star tracker located at the focal plane and a steerable mirror in the SIRTF optical path, has been designed to work in conjunction with the IPS. The CCD tracks multiple stars simultaneously and through the use of a high-performance microcomputer generates three-axis attitude errors and gyro drift estimates to correct the IPS gyros. A high-bandwidth feed-forward loop, driven directly from the IPS gyro package, controls the steering mirror in order to correct disturbances not compensated for by the IPS control system. The SIRTF IMC system is described in detail and performance is analyzed with respect to system noise inputs, environmental disturbances, and error sources such as bending and feed-forward scale factor. It is concluded that the SIRTF accuracy and stability requirements can be met with this design.			
17 Key Words (Suggested by Author(s)) Attitude control, Control system analysis, Discrete systems, Feed-forward, Microprocessors, Tracking systems		18. Distribution Statement Unlimited  STAR Category - 66	
19. Security Classif. (of this report) Unclassified	20. Security Classif. (of this page) Unclassified	21. No. of Pages 40	22 Price* \$4.50